2004.
21) Narita M, Nishigami N, Narita N, Yamaguti K, Okado N, Watanabe Y, Kuratsune H: Association between serotonin transporter gene polymorphism and chronic fatigue syndrome. Biochem Biophys Res Commun 311: 264–266, 2003.
22) Sasabe T, Kobayashi M, Kondo Y, Onoe H, Matsubara S, Yamamoto S, Tsukada H, Onoe K, Watabe H, Iida H, Kogo M, Sano K, Hatanaka A, Sawada T, Watanabe Y: Activation of the anterior cingulate gyrus by 'Green Odor': A positron emission tomography study in the monkey. Chem Senses 28: 565–572, 2003.
23) Fernell E, Watanabe Y, Adolfsson I, Tani Y, Bergström M, Lilja A, Hartvig P, von Knorring A-L, Gillberg C, Långström B: Possible effects of tetrahydrobiopterin treatment in six children with autism – clinical and positron emission tomography data: a pilot study. Dev Med Child Neurol 39: 313–318, 1997.
24) Danfors T, von Knorring A-L, Hartvig P, Langstrom B, Moulder R, Stromberg B, Torstenson R, Wester U, Watanabe Y, Eeg-Olofsson O: Tetrahydrobiopterin in the treatment of children with autistic disorder: a double-blind placebo-controlled crossover study. J Clin Psychopharmacol 25: 485–489, 2005.
25) Matsumura A, Mizokawa S, Tanaka M, Wada Y, Nozaki S, Nakamura F, Shiomi S, Ochi H, Watanabe Y: Assessment of microPET performance in analyzing the rat brain under different types of anesthesia: Comparison between quantitative data obtained with microPET and *ex vivo* autoradiography. Neuroimage 20: 2040–2050, 2003.

Innovative Molecular Imaging Research for Efficient Drug Development and Diagnosis

Yasuyoshi Watanabe[1,2], Masaaki Suzuki[1,3], Hirotaka Onoe[1], Hisashi Doi[1], Yasuhiro Wada[1], Yosky Kataoka[1,2], Shuichi Enomoto[1,4]

[1] Molecular Imaging Research Program, RIKEN
[2] Osaka City University Graduate School of Medicine
[3] Gifu University Graduate School of Medicine
[4] Metallomics Research Unit, RIKEN Wako Institute

IEEE TRANSACTIONS ON NUCLEAR SCIENCE, VOL. 54, NO. 3, JUNE 2007

Gamma-Ray Compton Imaging of Multitracer in Biological Samples Using Strip Germanium Telescope

Shinji Motomura, Shuichi Enomoto, Hiromitsu Haba, Kaori Igarashi, Yasuyuki Gono, and Yasushige Yano

Abstract—**The feasibility of using a Compton camera for multitracer imaging has been demonstrated with the results of two biological sample imaging experiments. The distribution of the multitracer administered to a soybean sample and a tumor-bearing mouse has been visualized for each nuclide simultaneously. Three-dimensional images of the multitracer have been obtained even though the samples were measured from a fixed direction.**

Index Terms—**Biomedical nuclear imaging, Compton camera, germanium radiation detectors, multitracer.**

I. Introduction

THE multitracer, which was invented at RIKEN in 1991 [1], is a powerful tool for investigating the behavior of various chemical elements in a sample. It is produced by irradiating a metal target with a heavy-ion beam accelerated to an energy of 135 MeV/u, and then chemically processing the various radioactive nuclides produced mainly through the nuclear-fragmentation reaction, into the final form of a multitracer solution. Since the multitracer contains the radioisotopes of various elements, the information regarding the radioisotopes under the same conditions can be obtained simultaneously by a single experiment. Moreover, the multitracer enables us to observe the correlated behavior among many elements. This information can never be obtained by combining the data of many single-tracer experiments. Owing to these advantages, the multitracer has found many applications in biology, medicine, environmental science, and other fields [2].

Although the potential advantages of multitracers are promising, no nondestructive inspection method has yet been established to realize their full potential particularly for in vivo imaging. This is because the multiple γ rays emitted from the multitracer span an energy range from ~100 keV to 2 MeV. For energies above ~300 keV, sufficient spatial resolution cannot be obtained by a conventional γ-ray imager equipped with mechanical collimators. In addition, the energy resolution must be high enough to distinguish each nuclide contained in the multitracer.

In this paper, we describe a prototype of a Compton camera for mutlitracer imaging, which we call GREI (Gamma-Ray Emission Imaging), and present some results of test experiments with biological samples. The original idea of the Compton camera was invented in the early 1970s [3], and it was soon proposed for medical imaging [4]. Since then, various types of Compton cameras have been proposed for various uses [5].

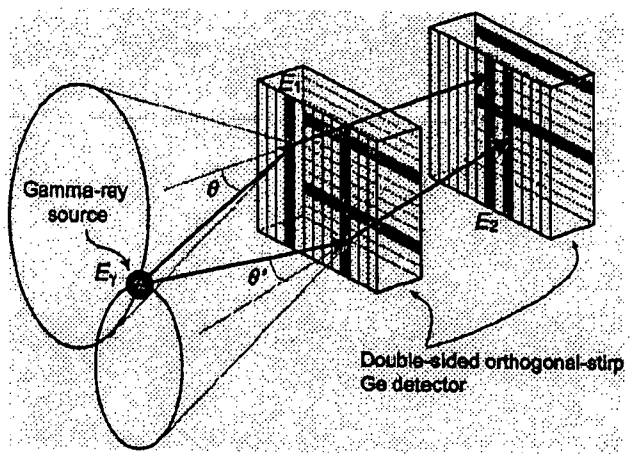

Fig. 1. Schematic of the strip Ge telescope operated as a Compton camera.

Previously, we performed a test experiment using a Compton camera composed of two segmented germanium (Ge) detectors [6]. Owing to the excellent energy resolution of the Ge detectors, three γ-ray sources of ^{60}Co, ^{137}Cs and ^{152}Eu were clearly distinguished by setting energy windows on the corresponding γ-ray photopeaks, and their positions were simultaneously determined. The GREI system described in this paper has been modified taking into account the results of the test experiment, further simulations [7], and recent technologies developed for γ-ray detection [8]–[12].

II. Description of the GREI System

The GREI system is composed of two double-sided orthogonal-strip Ge detectors manufactured by Eurisys Mesures (Fig. 1). The detectors are arranged parallel to each other and mounted in a single cryostat. The dimensions of the active volume of the Ge crystals are 39 mm × 39 mm × 10 mm and 39 mm × 39 mm × 20 mm for the front and rear detectors, respectively. The strip pitch is 3 mm for both detectors. The center-to-center distance between the crystals is 60 mm.

The electronics are schematically shown in Fig. 2. Conventional circuit modules based on NIM and CAMAC standards

Manuscript received November 14, 2004; revised January 24, 2007. This work was supported in part by the Special Postdoctoral Researchers Program of RIKEN.

The authors are with the Cyclotron Center, RIKEN, Wako, Saitama 351-0198, Japan (e-mail: motomura@riken.jp).

Digital Object Identifier 10.1109/TNS.2007.894209

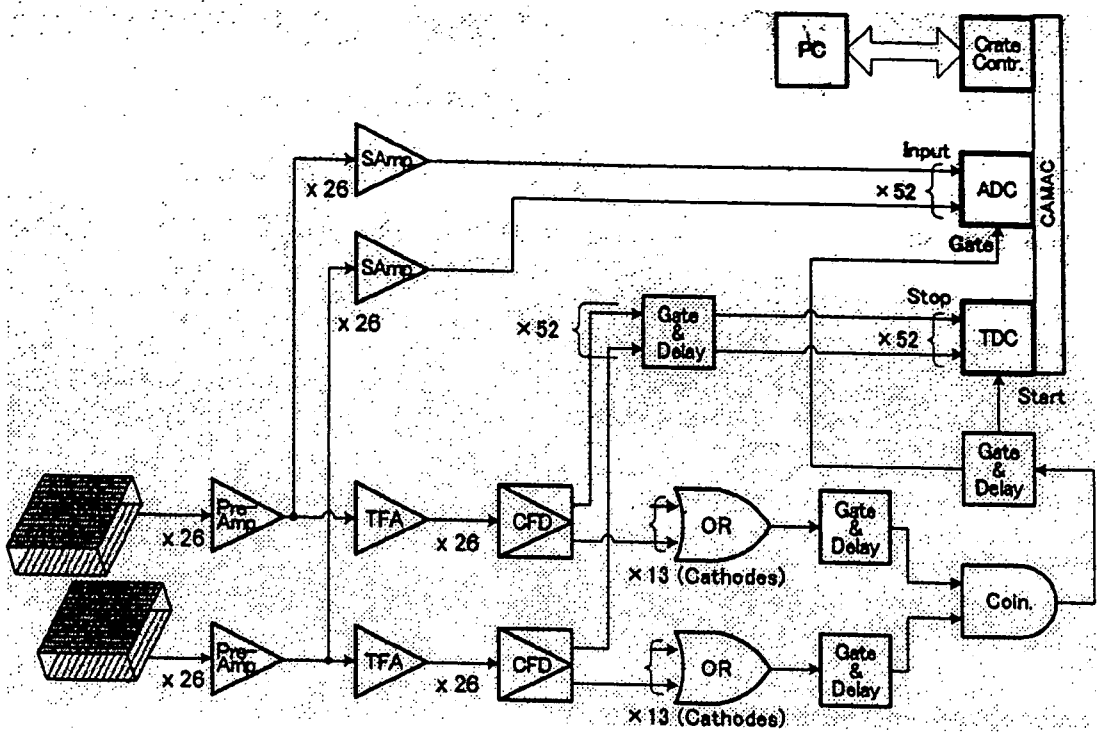

Fig. 2. Circuit diagram of the current prototype of the GREI system. The circuit modules are based on NIM and CAMAC standards.

are used. All the output signals of the preamplifiers are fed into the constant fraction discriminators (CFDs) through the timing filter amplifiers (TFAs), and the timing pulses are generated. All the timing pulses are fed into the time-to-digital converters (TDCs) to digitize the timing signals. To select the Compton scattering events, the timing pulses derived from the cathode strips are used to perform coincidence measurement between the front and rear detectors.

All the output signals of the preamplifiers are also fed into the shaping amplifiers to generate slow signals for energy measurement. Then the pulse heights are digitized by the analog-to-digital converters (ADCs).

In the current implementation, the transverse position of the γ-ray interaction is determined by a combination of the anode and cathode strips with the accuracy given by the width of the strip. On the other hand, the depth position of the γ-ray interaction in the Ge crystal can be determined more accurately than the thickness of the crystal, by taking into account the time difference between the signals from the anode and cathode strips [8]–[12]. To realize accurate depth measurement, the time constants of TFAs were set to 500 ns and 60 ns for differentiation and integration, respectively. Delay time of the CFDs was set to 50 ns, which was the upper limit of the modules, and the fraction of the CFDs was set to 0.5.

The digitized data of the TDCs and ADCs are transferred event by event to the personal computer. The transferred data are analyzed on-line, and also recorded in list mode for further off-line analysis. If an incident γ ray is Compton scattered in the front detector and deposits energy E_1, and then the scattered γ ray is fully absorbed in the rear detector and deposits energy E_2, the original γ-ray energy E_γ is obtained by summing E_1 and E_2. Thus, the nuclides contained in the multitracer are distinguished by setting energy windows at the corresponding energy peaks in the E_γ spectrum. Throughout this paper, the range of an energy window was $\pm$ 5 keV of the peak position and the windows were applied in the software.

III. Implementation of Image Reconstruction Methods

For image reconstruction, we are currently employing a two-step method. In the first step, an intermediate image, which is called a simple back-projection (SBP) image, is constructed by simply accumulating the back-projections over all detected events, using an algorithm analogous to the cone-surface mapping algorithm [13]. The back-projection for one event is a cone surface that indicates the possible position of the γ-ray source. The cone axis is the straight line passing through the first and second interaction points. The half-cone angle θ is the Compton scattering angle determined by the following equation:

$$\cos\theta = 1 + m_e c^2 \left(\frac{1}{E_\gamma} - \frac{1}{E_\gamma - E_1} \right), \qquad (1)$$

where $m_e c^2$ is the rest-mass energy of an electron.

Here, we adopt a model that the SBP image is constructed by linear mapping of the source distribution image; that is,

$$n_i = \sum_j p_{ij} \lambda_j, \qquad (2)$$

where n_i is the value of voxel i in the SBP image, λ_j is the value of voxel j in the source distribution image, p_{ij} is the point-spread function (PSF), or the point kernel function [13], which represents the SBP image of the point source at voxel j; the three-dimensional (3D) coordinates are represented by the single indices i and j. In general, the shape of the PSF varies depending on the source position, because the range of the accepted incident angle and scattering angle of γ rays depends on the source position. Therefore, a spatially variant PSF must be used to perform rigorous image reconstruction. However, the PSF should be approximated by a spatially invariant PSF within a local region.

Then the second step is to deconvolve the SBP image with the PSF. We have implemented an analytical algorithm and an iterative algorithm for the deconvolution.

If the PSF is assumed to be spatially invariant, λ_j can be reconstructed analytically by adopting the Fourier convolution theorem. The matrix p_{ij} is diagonalized by taking the Fourier transform of both sides of (2), and then λ_j is obtained in the spatial frequency domain as follows:

$$\lambda_j = \frac{n_j}{p_{jj}}. \tag{3}$$

In most cases, an additional filter function (w_j) must be multiplied to the right side of (3) in order to suppress the statistical noise components, which are dominant in the high-frequency regions, that is:

$$\lambda_j = \frac{w_j n_j}{p_{jj}}. \tag{4}$$

If a Wiener filter function can be designed for the system, (4) becomes the optimal estimation in terms of the least square errors. In addition, ad hoc filter functions, such as a Butterworth function, can be used for w_j to suppress the noise components in the high-frequency regions.

We have also implemented an iterative deconvolution algorithm, which was adapted from the additive SIRT algorithm [14]. First, an initial estimate of the original image $\lambda_j^{(0)}$ is obtained by averaging the SBP image:

$$\lambda_j^{(0)} = \frac{1}{N}\sum_{i=1}^{N} n_i. \tag{5}$$

Then the (n+1)-th estimate ($\lambda_j^{(n+1)}$) is obtained from the n-th estimate ($\lambda_j^{(n)}$) as follows:

$$\lambda_j^{(n+1)} = \lambda_j^{(n)} + \sum_i \left(n_i - \sum_k \lambda_k^{(n)} p_{ik} \right) p_{ij}. \tag{6}$$

Although spatially variant PSFs can be used for p_{ij}, spatially invariant PSFs have been used in the current work.

A close examination shows that (6) is the iteration term that minimizes the square errors of the SBP image constructed from the estimated source distribution. This can be seen if we recast the steepest descent iteration term from [15]:

$$\begin{aligned}\Delta\lambda_j^{(n)} &= -\varepsilon \nabla \chi^2 \left(\lambda_j^{(n)}\right) \\ &= -\varepsilon \frac{\sum_i \partial \left(n_i - \sum_k \lambda_k^{(n)} p_{ik} \right)^2}{\partial \lambda_j^{(n)}} \\ &= 2\varepsilon \sum_i \left(n_i - \sum_k \lambda_k^{(n)} p_{ik} \right) p_{ij},\end{aligned} \tag{7}$$

where $\Delta\lambda_j^{(n)}$ is the displacement of the estimate in the iteration step, ϵ is a positive coefficient used to control the iteration. When $\epsilon = 0.5$, the second term on the right-hand side of (6) is obtained.

Since the PSF has a 3D distribution, 3D deconvolution must be performed in order to reconstruct 3D images. However, when the source distribution can be considered to be two-dimensional (2D), corresponding to the case of a sliced sample, 2D deconvolution is sufficient because there is no contamination from outside of the 2D plane. Thus, we have implemented both 2D and 3D deconvolution algorithms.

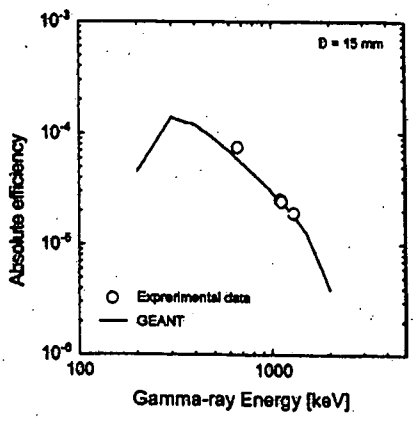

Fig. 3. Absolute efficiencies for obtaining the full-energy γ-ray peaks.

TABLE I
SPATIAL RESOLUTION OF THE RECONSTRUCTED IMAGE AND DERIVED TRANSITIONAL SPATIAL FREQUENCY OF THE FPSD OF THE SBP IMAGE

Number of events	FWHM [mm]		f_c [mm^{-1}]	
	x-direction	z-direction	x-direction	z-direction
1.0×10^3	4.9	11.4	0.16±0.02	0.06±0.01
5.0×10^4	6.0	12.9	0.15±0.02	0.05±0.01
1.0×10^4	10.3	14.2	0.12±0.03	0.04±0.01

IV. PERFORMANCE OF THE PROTOTYPE

The absolute efficiencies for obtaining the full-energy γ-ray peaks from the sources 15 mm away from the center of the front detector are shown in Fig. 3, together with the values estimated by Monte Carlo simulation using a GEANT [16] code. The experimental values were derived from the experimental data mentioned in the next section. One can see that the GREI system has

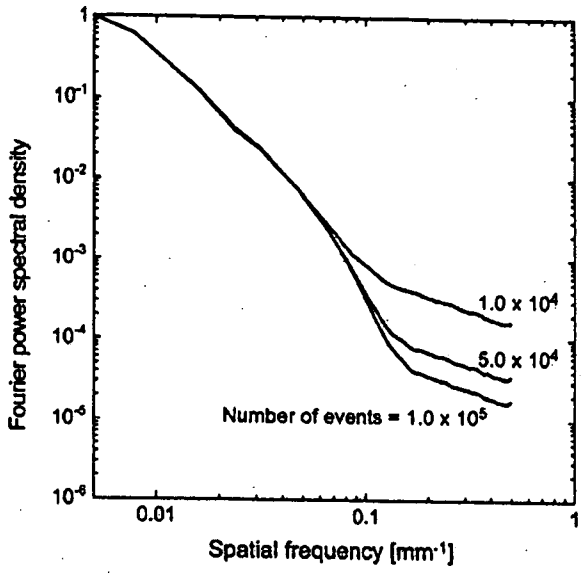

Fig. 4. Projection of the Fourier power spectral densities of the SBP images obtained by measuring ^{65}Zn point-like source using the GREI system.

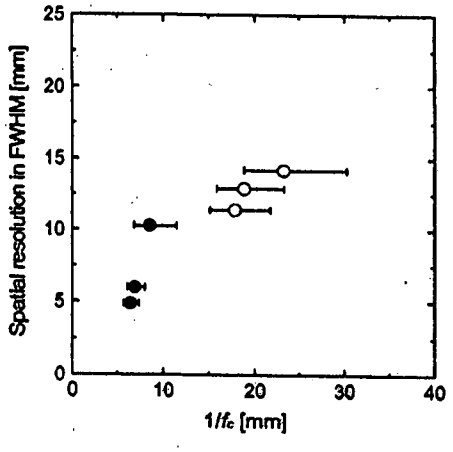

Fig. 5. Spatial resolution vs. $1/f_c$. Solid circle: x-direction, Open circle: z-direction.

significant efficiency between the energy range from ~200 keV to ~2 MeV.

The effect of the statistical noise on the spatial resolution achieved with the prototype system was investigated in terms of the Fourier power spectral density (FPSD) of the SBP image. A point-like source of ^{65}Zn, which emits 1116 keV γ rays, was placed 69 mm away from the center of the front detector, and then three SBP images were constructed in 3D space with the detected event numbers of 1.0×10^4, 5.0×10^4, and 1.0×10^5. Then the SBP images were analytically deconvolved with the PSF constructed using a GEANT code. The full widths at half maximum (FWHMs) of the reconstructed images of the point source are shown in Table I for each number of events. Fig. 4 shows the projection of the FPSDs onto the x-axis for the SBP images. One can see in the figure that there is a common component that decreases as the spatial frequency increases. This component is understood to represent the intrinsic characteristics of the GREI system. One can also see in Fig. 4 that there

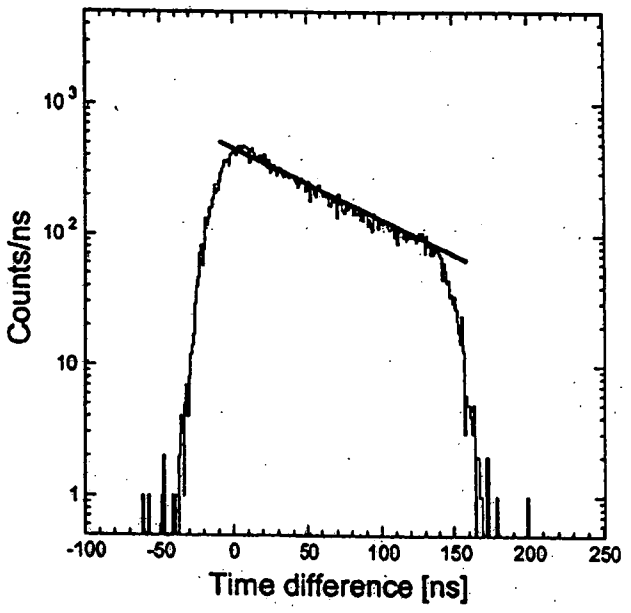

Fig. 6. Histogram of the time difference between the signals of the anode and cathode strips. The energy window was set at the 122-keV γ-ray peak of ^{152}Eu. The solid line indicates a fit using an exponential function.

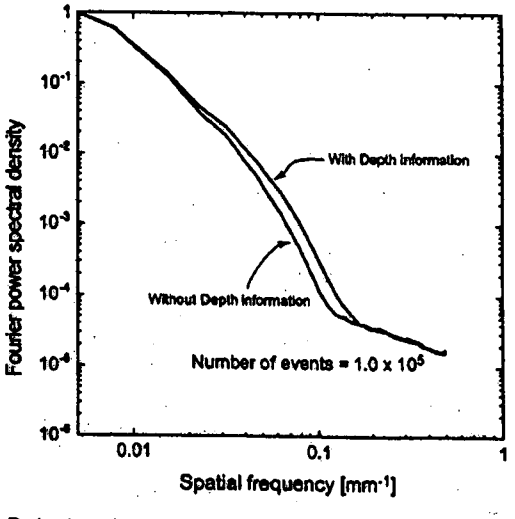

Fig. 7. Projection of the Fourier power spectral densities of the SBP images obtained by measuring ^{65}Zn point-like source using the GREI system.

is another component significant in the high-frequency region, which is understood to be the statistical noise component because it decreases as the number of events increases. We defined the transitional spatial frequency f_c (Table I), where the noise component is beginning to be dominant, by the positive peak of the second derivative of the FPSD curve. As a function of $1/f_c$, the spatial resolutions are plotted in Fig. 5. In the figure, one can see a positive correlation between the spatial resolution and $1/f_c$. However, the correlations for x- and z-direction seem to differ. If we can obtain the comprehensive relationship between the spatial resolution and $1/f_c$, the information would be useful to estimate the performance of the designed system without image reconstruction.

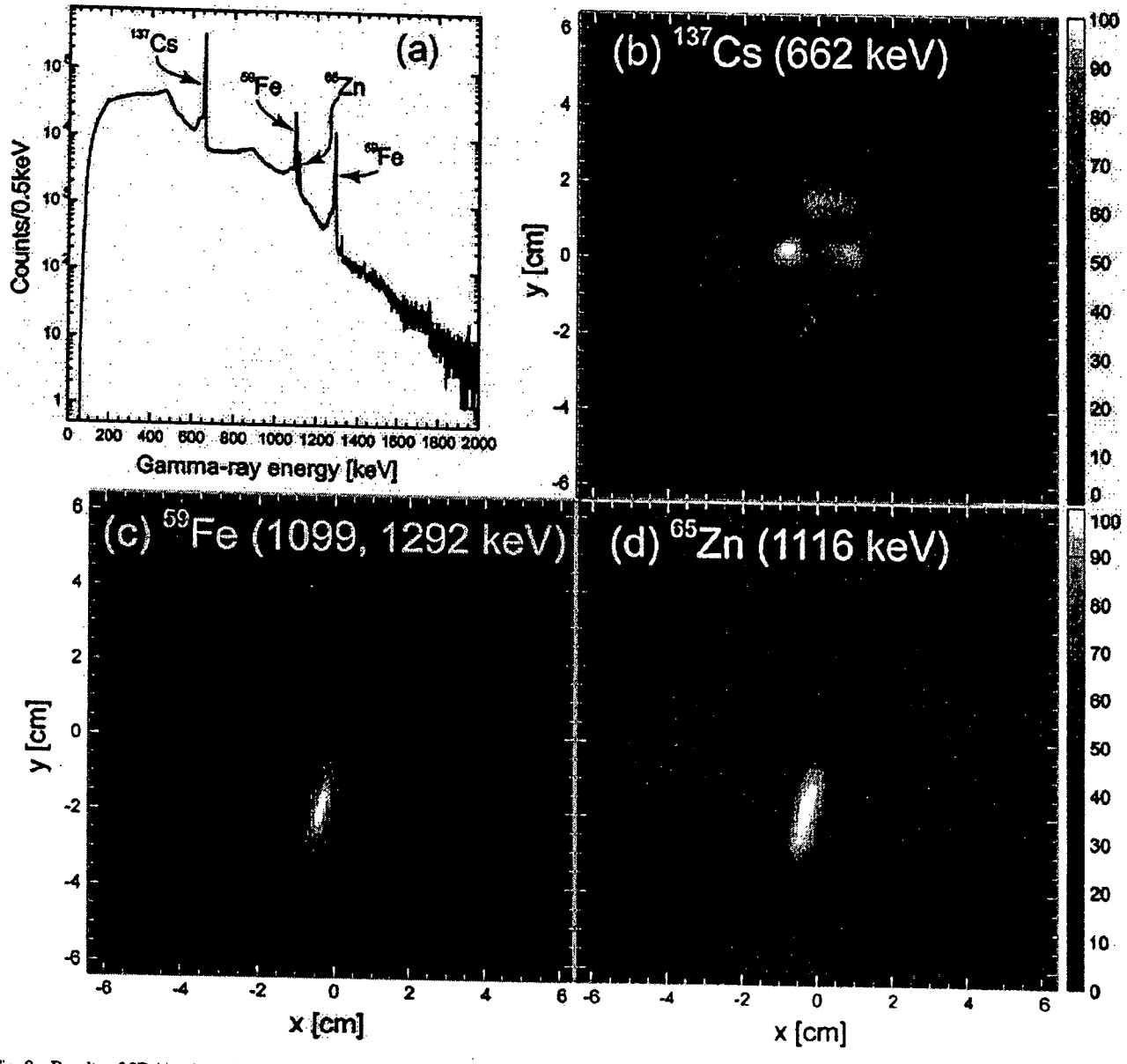

Fig. 8. Results of 2D imaging of the soybean sample.

In order to derive the depth position of the interaction from the time difference between the anode and cathode signals, the time difference was measured for each combination of the anode and cathode strips using a γ-ray source of ^{152}Eu placed in front of the detector. Fig. 6 shows one of the histograms for the front detector with an energy window at the 122-keV γ-ray peak. The origin of the abscissa has been adjusted so that the time difference is 0 ns when the counts are maximum. The dependence of the counts on the time difference agreed well with the attenuation curve of 122-keV γ rays in Ge crystals assuming that the time differences of 0 ns and 140 ns correspond to the depth positions of 0 mm and 10 mm, respectively. Considering this fact, we assigned a simple linear function of the time difference to derive the depth position; the position resolution is determined by the quality of the fit and the time resolution. Moreover, the spread of the timing spectrum was found to be identical even for the other γ-ray energies. Owing to this fact, the algorithm to derive the depth position has become very simple. This is an advantage of using CFDs, which generate the timing pulses independent of the amplitude of the input signals.

The effect of the depth measurement was examined in terms of the FPSD as mentioned above. Two SBP images were constructed with and without the depth information using the same data shown in Fig. 4 with 1.0×10^5 events. The FPSDs of the SBP images are shown in Fig. 7. One can see that the intrinsic characteristics of the system deteriorated without the depth information, though the statistical noise was of the same level. This result was consistent with the Monte Carlo simulation where the position resolution of depth measurement was 1 mm in FWHM.

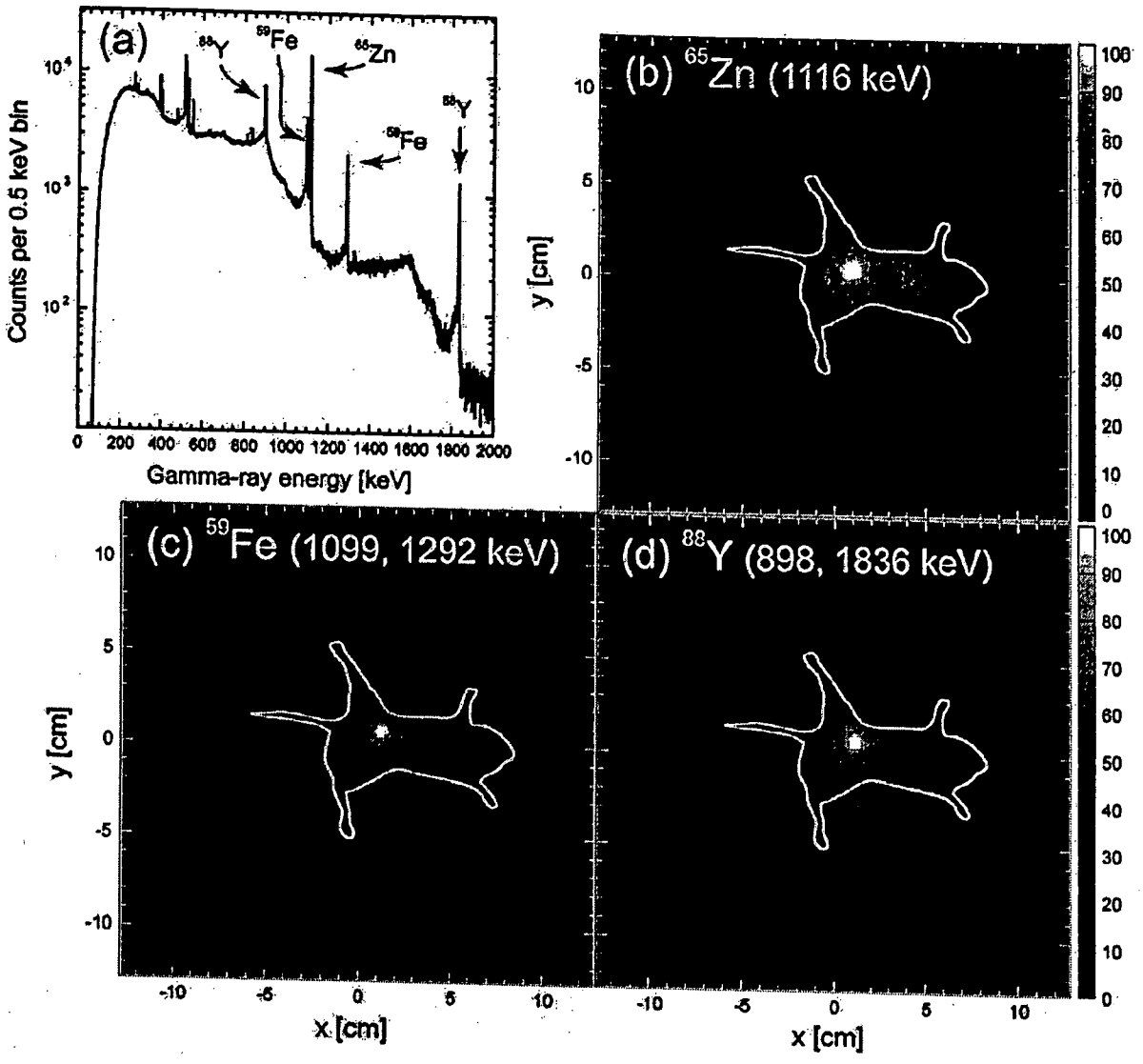

Fig. 9. Results of 2D imaging of the tumor-bearing mouse.

V. Experiment With Biological Samples

We have performed experiments with two biological samples in order to demonstrate the capability of nondestructive imaging of a multitracer. The first sample was a soybean plant administered with 310-kBq ^{137}Cs, 89-kBq ^{59}Fe, and 20-kBq ^{65}Zn. A photograph of the sample is shown in Fig. 10. The sample was fixed on a plane 15 mm away from the center of the front Ge detector. The measurement was carried out for 25 hours.

Fig. 8 shows the results of 2D imaging of the soybean sample. The energy windows were set at each peak position indicated in the γ-ray energy spectrum Fig. 8 to distinguish the radionuclides of ^{137}Cs, ^{59}Fe, and ^{65}Zn. The 2D SBP images were constructed for each nuclide on the plane where the sample was fixed, assuming a 2D distribution, and then the analytical reconstruction method was used to deconvolve the 2D SBP images with the 2D PSFs. The resulting images successfully visualized the different behaviors of the nuclides. The ^{137}Cs nuclide was distributed throughout the whole of the sample, because it is chemically analogous to K, while ^{59}Fe and ^{65}Zn remained near the root. The ^{65}Zn nuclide was found at the tip of the stem to some extent, where the plant was actively growing, because Zn is required for cell division.

In addition, we note that there is a difference in the background structure of the images. This is due to the difference in the number of events obtained for each nuclide; 2.5×10^6, 3.4×10^5, and 7.3×10^4 for ^{137}Cs, ^{59}Fe, and ^{65}Zn, respectively. The smaller the number of events, the larger the statistical noise component becomes, as mentioned in Section IV.

The second sample was a tumor-bearing mouse administered intravenously with a multitracer solution that includes 60-kBq ^{65}Zn, 30-kBq ^{59}Fe, and 10-kBq ^{88}Y. The sample was fixed on a board and placed just under the front detector, which was installed with its front face down. The measurement was carried out for 95 hours.

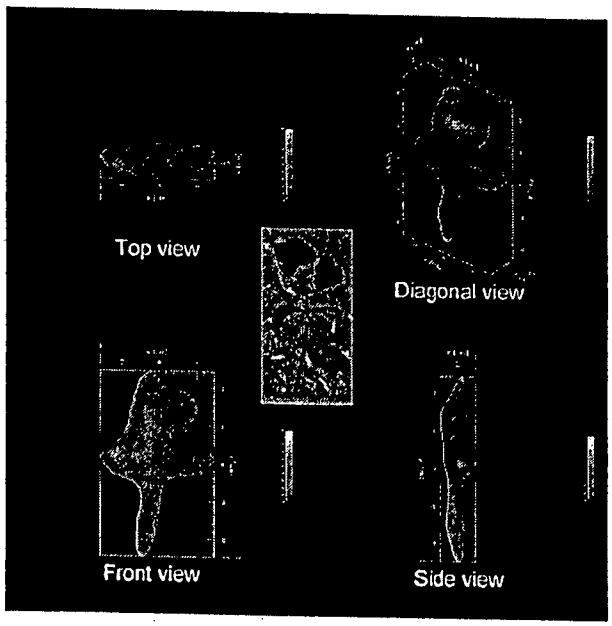

Fig. 10. Three-dimensional image of ^{137}Cs distributed in the soybean sample. A photograph of the sample is also shown at the center.

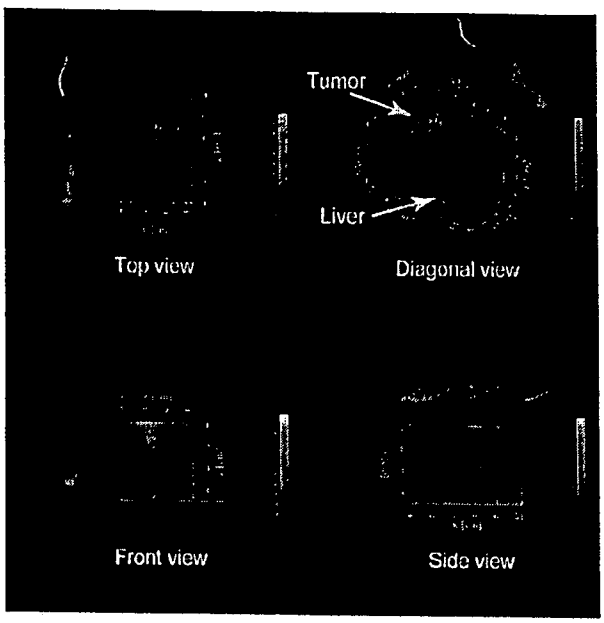

Fig. 11. Three-dimensional image of ^{65}Zn distributed in the tumor-bearing mouse. The orientations of the sample are indicated by the mouse figures.

Fig. 9 shows the results of 2D imaging of the tumor-bearing mouse. As in the case of the soybean sample, the energy windows were set at each peak position indicated in the γ-ray energy spectrum Fig. 9 to distinguish the radionuclides of ^{65}Zn, ^{59}Fe, and ^{88}Y. Then the 2D SBP images were constructed for each nuclide on the 2D plane that intersects the tumor part, and the SBP images were analytically deconvolved with the 2D PSFs. The resulting images are only "focused" images along the assumed plane, because the other parts of the sample have some contribution to the constructed 2D SBP images. Nevertheless, the accumulation of the nuclides in the tumor site was evident and ^{65}Zn was also found in the liver. The results are consistent with those reported in [17]–[19].

We have performed 3D imaging of these samples, even though the samples were measured from a fixed direction. When the sample is sufficiently close to the front detector, the source distribution can be projected towards various directions because no mechanical collimator is used. This is a distinctive feature of a Compton camera. First, the 3D SBP images were constructed in 3D space, then the SBP images were deconvolved with the 3D PSFs.

Fig. 10 shows the result of 3D imaging of ^{137}Cs in the soybean sample. The deconvolution was performed analytically. Since ^{137}Cs was distributed throughout the whole sample, the shape of the sample can be recognized. However, there exists a warp in the reconstructed image, which may have been caused by the use of spatially invariant PSFs.

Fig. 11 shows the result of 3D imaging of ^{65}Zn in the tumor-bearing mouse. In this case, we could not obtain any satisfactory images by analytical deconvolution. Thus, the reconstructed space was limited to only the region around the sample, and the iterative deconvolution was performed. The resulting image successfully visualized the accumulation of ^{65}Zn in the tumor and the liver. However, the image has a similar warp to the 3D image of the soybean sample. Spatially variant PSFs should be incorporated to obtain more accurate images.

We were able to demonstrate the feasibility of using the GREI system for nondestructive imaging of multitracer. However, the measurement times taken to obtain the images would be unsuitable for practical imaging, although they can be shortened to about 10 hours if more intense γ-ray sources are used. Moreover, a higher spatial resolution would be desired to observe more fine structure. These demands would be met if the γ-ray tracking technique and pulse-shape analysis are implemented, which have been recently developed [20]. With these techniques implemented, the efficiency and the intrinsic characteristics are improved, thereby shortening the measurement time and improving the spatial resolution.

VI. Summary

A prototype of a Compton camera, GREI, has been fabricated for nondestructive imaging of a multitracer. It is composed of two double-sided orthogonal-strip Ge detectors, and the efficiency is significant in the energy range from ~200 keV to 2 MeV. The timing method was used to derive the depth position of the γ-ray interaction with a resolution of ~1 mm FWHM. Both analytical and iterative image reconstruction methods were implemented for 2D and 3D imaging. A test experiment was performed to demonstrate the capability of the GREI system. The resulting images successfully visualized the different behavior of each nuclide for both the soybean and the mouse sample. Furthermore, 3D images were obtained even though the samples were measured from a fixed direction. However, there was some distortion in the 3D images, which may have been caused by the use of spatially invariant PSFs. Spatially variant PSFs should be incorporated to obtain more accurate 3D images. To make the GREI system suitable for practical imaging, γ-ray tracking technique and pulse-shape analysis should be implemented.

REFERENCES

[1] S. Ambe, S. Y. Chen, Y. Ohkubo, Y. Kobayashi, M. Iwamoto, M. Yanokura, and F. Ambe, "Preparation of a radioactive multitracer solution from gold foil irradiated by 135 MeV/nucleon ^{14}N ions," *Chem. Lett.*, pp. 149–152, 1991.

[2] S. Enomoto, "Development of multitracer technology and application studies on biotrace element research," *Biomed. Res. Trace Elem.*, vol. 16, pp. 233–240, 2005.

[3] V. Schönfelder, "A telescope for soft gamma ray astronomy," *Nucl. Instrum. Methods*, vol. 107, pp. 385–394, 1973.

[4] R. W. Todd, J. M. Nightingale, and D. B. Everett, "A proposed γ camera," *Nature*, vol. 251, pp. 132–134, 1974.

[5] G. W. Phillips, "Gamma-ray imaging with Compton cameras," *Nucl. Instrum. Methods Phys. Res. B*, vol. B99, pp. 674–677, 1995.

[6] Y. F. Yang, Y. Gono, S. Motomura, S. Enomoto, and Y. Yano, "A Compton camera for multitracer imaging," *IEEE Trans. Nucl. Sci.*, vol. 48, no. 3, pp. 656–661, Jun. 2001.

[7] Y. F. Yang, Y. Gono, S. Motomura, S. Enomoto, and Y. Yano, "Monte Carlo simulations of the performance of a Compton camera consisting of position sensitive germanium detectors," *Nucl. Instrum. Methods Phys. Res. A*, vol. A482, pp. 806–813, 2002.

[8] M. Momayezi, W. K. Warburton, and R. Kroeger, "Position resolution in a Ge-strip detector," *Proc. SPIE*, vol. 3768, pp. 530–537, 1999.

[9] M. Amman and P. N. Luke, "Three-dimensional position sensing and field shaping in orthogonal-strip germanium gamma-ray detectors," *Nucl. Instrum. Methods Phys. Res. A*, vol. A452, pp. 155–166, 2000.

[10] E. A. Wulf, J. Ampe, W. N. Johnson, R. A. Kroeger, J. D. Kurfess, and B. F. Phlips, "Depth measurement in a germanium strip detector," *IEEE Trans. Nucl. Sci.*, vol. 49, no. 4, pp. 1876–1880, Aug. 2002.

[11] E. A. Wulf, B. F. Phlips, W. N. Johnson, R. A. Kroeger, J. D. Kurfess, and E. I. Novikova, "Germanium strip detector Compton telescope using three-dimensional readout," *IEEE Trans. Nucl. Sci.*, vol. 50, no. 4, pp. 1182–1189, Aug. 2003.

[12] S. Motomura, S. Enomoto, Y. Gono, and Y. Yano, "Effect of electrode design on depth-of-interaction sensitivity in two-dimensionally segmented planar germanium detectors," to be submitted.

[13] R. C. Rohe, M. M. Sharfi, K. A. Kecevar, J. D. Valentine, and C. Bonnerave, "The spatially-variant backprojection point kernel function of an energy-subtraction Compton scatter camera for medical imaging," *IEEE Trans. Nucl. Sci.*, vol. 44, no. 6, pp. 2477–2482, Dec. 1997.

[14] P. Gilbert, "Iterative methods for the three-dimensional resonstruction of an object from projections," *J. Theor. Biol.*, vol. 36, pp. 105–117, 1972.

[15] W. H. Press, S. A. Teukolsky, W. T. Vetterling, and B. P. Flannery, *Numerical Recipes in C: The Art of Scientific Computing*, 2nd ed. Cambridge, U.K.: Cambridge Univ. Press, 1992, p. 681.

[16] Detector Description and Simulation Tool, GEANT, CERN, Geneva, 1993.

[17] H. Tamano, S. Enomoto, B. Liu, and A. Takeda, "Tumor accumulation of radioactive trace elements: A multitracer study," *Biomed. Res. Trace Elem.*, vol. 12, pp. 96–101, 2001.

[18] H. Tamano, S. Enomoto, N. Oku, and A. Takeda, "Preferential uptake of zinc, manganese and rubidium in rat brain tumor," *Nucl. Med. Biol.*, vol. 29, pp. 505–508, 2002.

[19] A. Takeda, H. Tamano, S. Enomoto, and N. Oku, "Zinc-65 imaging of rat brain tumors," *Cancer Res.*, vol. 61, pp. 5065–5069, 2001.

[20] K. Vetter, M. Burks, and L. Mihailescu, "Gamma-ray imaging with position-sensitive HPGe detectors," *Nucl. Instrum. Methods Phys. Res. A*, vol. A525, pp. 322–327, 2004.

Chemistry Letters Vol.37, No.3 (2008)

Fluoride Complexation of Element 104, Rutherfordium (Rf), Investigated by Cation-exchange Chromatography

Yasuo Ishii,*[1,2] Atsushi Toyoshima,[1] Kazuaki Tsukada,[1] Masato Asai,[1] Hayato Toume,[1] Ichiro Nishinaka,[1] Yuichiro Nagame,[1] Sunao Miyashita,[2] Tomotaka Mori,[2] Hideo Suganuma,[2] Hiromitsu Haba,[3] Masami Sakamaki,[4] Shin-ichi Goto,[4] Hisaaki Kudo,[4] Kazuhiko Akiyama,[5] Yasuji Oura,[5] Hiromichi Nakahara,[5] Yuki Tashiro,[6] Atsushi Shinohara,[6] Matthias Schädel,[7] Willy Brüchle,[7] Valeria Pershina,[7] and Jens V. Kratz[8]

[1]*Advanced Science Research Center, Japan Atomic Energy Agency (JAEA), Tokai, Ibaraki 319-1195*
[2]*Radiochemical Research Laboratory, Shizuoka University, Shizuoka 422-8529*
[3]*Nishina Center for Accelerator Based Science, RIKEN, Wako 351-0198*
[4]*Department of Chemistry, Niigata University, Niigata 950-2181*
[5]*Graduate School of Science and Engineering, Tokyo Metropolitan University, Hachioji, Tokyo 192-0397*
[6]*Graduate School of Science, Osaka University, Toyonaka, Osaka 560-0043*
[7]*Gesellschaft für Schwerionenforschung, D-64291 Darmstadt, Germany*
[8]*Institut für Kernchemie, Universität Mainz, D-55099 Mainz, Germany*

(Received December 6, 2007; CL-071354; E-mail: ishii.yasuo@jaea.go.jp)

We report on new and much more precise cation-exchange data of element 104, rutherfordium (Rf), in the fluoride ion concentration [F^-] range of 5.29×10^{-5}–1.04×10^{-3} M. The result based on one-atom-at-a-time chemistry clearly demonstrates that the distribution coefficients (K_d) decrease with increasing [F^-], suggesting successive fluoride complexation of Rf. The complexation of Rf is briefly discussed in terms of fully relativistic density functional calculation theory.

Chemical characterization of the transactinide elements with atomic numbers $Z \geq 104$ is an extremely fascinating and challenging subject in modern nuclear and inorganic chemistry.[1] Most important and interesting question is to clarify chemical properties of these newly synthesized elements at the uppermost end of the periodic table and to elucidate the influence of relativistic effects in chemical properties of the heaviest elements.[2] The transactinide elements are produced at accelerators in heavy-ion-induced nuclear reactions. Because of the short nuclear half-lives ($T_{1/2}$) and extremely low production rates, however, chemical experiments must be done on an atom-at-a-time scale.

In our previous works,[3–6] fluoride complexation of Rf belonging to the group-4 elements was investigated through anion- and cation-exchange chromatography together with the lighter homologues Zr and Hf in hydrofluoric acid (HF) and in hydrofluoric and nitric acid (HF/HNO_3) mixed solutions. These results revealed that the ion-exchange behavior of Rf is remarkably different from that of Zr and Hf and that the fluoride complexation of Rf is much weaker than that of the homologues. In this report, new and more precise cation-exchange data of Rf in HF/0.1 M HNO_3 solution are presented to investigate the consecutive fluoride complex formation of Rf and to discuss the strength of the fluoride complexation of Rf and the homologues Zr and Hf together with the tetravalent pseudo homologue Th by comparing with the fully relativistic density functional calculation.

The experimental procedures are basically the same as those in the previous studies.[4,6] The nuclide ^{261}Rf ($T_{1/2} = 78$ s) was synthesized in the ^{248}Cm(^{18}O, 5*n*) reaction with a rate of about 2 atoms per minute at the JAEA tandem accelerator.[7] Reaction products recoiling from the target foil were stopped in He gas loaded with potassium chloride (KCl) aerosols. The products adsorbed on the surface of the aerosols were continuously transported through a capillary (2.0 mm i.d. × 20 m) to the chemistry laboratory within a few seconds. Cation-exchange experiments of Rf were conducted using the automated rapid ion-exchange separation apparatus AIDA that enables us to perform cyclic column chromatographic separations.[4–6] The transported products were collected on the deposition site of AIDA for 130 s. Then, the products were dissolved with 250 μL of the mixed HF/0.1 M HNO_3 solutions, [HF] = 5.00×10^{-3}, 1.30×10^{-2}, 2.50×10^{-2} and 1.00×10^{-1} M ([F^-] = 5.29×10^{-5}, 1.37×10^{-4}, 2.63×10^{-4} and 1.04×10^{-3} M, respectively[8]) and were subsequently fed onto the micro columns (1.6 mm i.d. × 7.0 mm and 1.0 mm i.d. × 3.5 mm) filled with the cation-exchange resin MCI GEL CK08Y (particle size of 25 μm) at a flow rate of 0.7 mL min^{-1}. The effluent was collected on a Ta disk as fraction 1. The remaining products in the column were stripped with 250 μL of 0.1 M HF/0.1 M HNO_3 at a flow rate of 1.0 mL min^{-1} and the effluent was collected on another Ta disk as fraction 2. Both samples were evaporated to dryness using hot He or N_2 gas and a halogen heat lamp. The pair of disks was automatically transferred to an α-spectrometry station to identify the nuclide through its α-decay energy. The above procedures were repeated more than 800 times. From the radioactivities observed in fractions 1 and 2, the adsorption probability on the cation-exchange resin was determined. The ^{248}Cm target contained Gd (39.3%-enriched ^{152}Gd) to simultaneously produce the short-lived ^{169}Hf ($T_{1/2} = 3.42$ min) through the Gd(^{18}O, *xn*) reaction. After the α-particle measurement, every third pair of disks was sampled and assayed by γ-ray spectrometry to monitor the chemical yield and adsorption behavior of ^{169}Hf. The chemical yield was approximately 60%.

The K_d values of the Zr, Hf and Th in 1.0×10^{-4}–1.0 M HF ([F^-] = 1.04×10^{-6}–1.04×10^{-2} M)/0.1 M HNO_3 on the same resin CK08Y were separately measured by a batch-wise method using the radiotracers of ^{88}Zr, ^{175}Hf and ^{234}Th. The elution behavior of ^{85}Zr and ^{169}Hf produced in the ^{nat}Ge(^{18}O, *xn*) and ^{nat}Gd(^{18}O, *xn*) reactions, respectively, were also investigated with AIDA in 5.0×10^{-4}–2.0×10^{-3} M HF ([F^-] = 5.29×10^{-6}–2.12×10^{-5} M)/0.1 M HNO_3 to com-

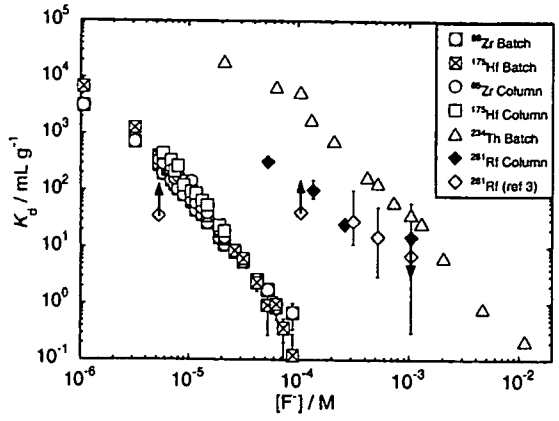

Figure 1. Distribution coefficients (K_d) of Zr, Hf, Th, and Rf on the cation-exchange resin (CK08Y) in 0.1 M HNO_3 depending on the concentration of the fluoride ion [F^-]. Also shown are K_d values of Rf (◇) taken from ref 3.

pare the K_d values obtained from column chromatography to those by the batch method.

Figure 1 shows the cation-exchange behavior of Zr, Hf, Th and Rf in HF/0.1 M HNO_3 as a function of [F^-]. The K_d values of ^{85}Zr and ^{169}Hf by the column chromatography agree well with those by the batch-wise method, indicating that the chemical reactions in the column method reach equilibrium. The K_d values of Zr, Hf, and Th decrease with increasing [F^-]. This feature, as being reported in refs 9–11 for the determination of the stability constants of fluoride complexes of these elements, shows the consecutive formation of the fluoride complexes. The K_d values of Rf were evaluated from the adsorption probability values by assuming that the reaction kinetics in the fluoride complexation and ion-exchange processes of Rf are as fast as those for Zr and Hf.[4–6] It is clearly found that the K_d values of Rf also decrease with the increasing [F^-] being between those of Zr/Hf and Th. The values of K_d for Rf under similar conditions were reported in ref 3 and the trend fits well to the present data as shown in Figure 1, although the previous data[3] show large statistical errors. These results suggest that the fluoride complex formation of Rf successively proceeds in the same way as for the homologues. Further, the present data unequivocally indicate that the fluoride complexation of Rf is significantly weaker than that of Zr and Hf, but it is stronger than the complexation of Th.

The observed cation-exchange data of the group-4 complexes are in full agreement with the theoretical prediction.[13] In ref 13 free energy changes of the complex formation reactions were determined on the basis of the fully relativistic density functional theory calculations of the electronic structures of various hydrated, hydrolyzed and fluoride complexes of Zr, Hf and Rf. It was shown that at lower HF concentrations the strength of the formed complexes has the following trend in group 4: Zr ≥ Hf > Rf. This causes the following trend in the K_d values: Zr ≤ Hf < Rf (see ref 13 for the explanation). It was also shown that because of the predominant electrostatic interaction one could observe a correlation (a reverse dependence) between the crystallographic ionic radii (IRs) and the strengths of the formed complexes and, hence, a correlation between the former and K_d values, which is valid only for the sorption of cationic complexes. The IRs of these elements change in the order of Zr (72 pm) ≈ Hf (71 pm) < Rf (76 pm) ≪ Th (94 pm) (see ref 12 for Zr, Hf and Th, and ref 2 for Rf), which in this particular case correlates (in the reversed order) with the sequence in the complex formation Zr ≈ Hf > Rf > Th.

Thus, in agreement with the theory, it was shown here experimentally that the strength of the fluoride complex formation Rf is weaker than those of Zr and Hf and stronger than that of Th.

References and Notes

1 M. Schädel, *Angew. Chem., Int. Ed.* **2006**, *45*, 368; M. Schädel, *The Chemistry of Superheavy Elements*, Kluwer, Dordrecht, **2003**.

2 V. G. Pershina, *Chem. Rev.* **1996**, *96*, 1977; V. Pershina, in *The Chemistry of Superheavy Elements*, ed. by M. Schädel, Kluwer, Dordrecht, **2003**, Chap. 2, pp. 31–94.

3 E. Strub, J. V. Kratz, A. Kronenberg, A. Nähler, P. Thörle, S. Zauner, W. Brüchle, E. Jäger, M. Schädel, B. Schausten, E. Schimpf, Li. Zongwei, U. Kirbach, D. Schumann, D. Jost, A. Türler, M. Asai, Y. Nagame, M. Sakama, T. Tsukada, H. W. Gäggeler, J. P. Glatz, *Radiochim. Acta* **2000**, *88*, 265; J. V. Kratz, in *The Chemistry of Superheavy Elements*, ed. by M. Schädel, Kluwer, Dordrecht, **2003**, Chap. 5, pp. 159–203.

4 H. Haba, K. Tsukada, M. Asai, A. Toyoshima, K. Akiyama, I. Nishinaka, M. Hirata, T. Yaita, S. Ichikawa, Y. Nagame, K. Yasuda, Y. Miyamoto, T. Kaneko, S. Goto, S. Ono, T. Hirai, H. Kudo, M. Shigekawa, A. Shinohara, Y. Oura, H. Nakahara, K. Sueki, H. Kikunaga, N. Kinoshita, N. Tsuruga, A. Yokoyama, M. Sakama, S. Enomoto, M. Schädel, W. Brüchle, J. V. Kratz, *J. Am. Chem. Soc.* **2004**, *126*, 5219.

5 A. Toyoshima, H. Haba, K. Tsukada, M. Asai, K. Akiyama, I. Nishinaka, Y. Nagame, D. Saika, K. Matsuo, W. Sato, A. Shinohara, H. Ishizu, M. Ito, J. Saito, S. Goto, H. Kudo, H. Kikunaga, N. Kinoshita, C. Kato, A. Yokoyama, K. Sueki, *J. Nucl. Radiochem. Sci.* **2004**, *5*, 45.

6 A. Toyoshima, H. Haba, K. Tsukada, M. Asai, K. Akiyama, S. Goto, W. Sato, Y. Ishii, I. Nishinaka, T. K. Sato, Y. Nagame, Y. Tani, H. Hasegawa, K. Matsuo, D. Saika, Y. Kitamoto, A. Shinohara, M. Ito, J. Saito, H. Kudo, A. Yokoyama, M. Sakama, K. Sueki, Y. Oura, H. Nakahara, M. Schädel, W. Brüchle, J. V. Kratz, *Radiochim. Acta* in press.

7 Y. Nagame, M. Asai, H. Haba, S. Goto, K. Tsukada, I. Nishinaka, K. Nishio, S. Ichikawa, A. Toyoshima, K. Akiyama, H. Nakahara, M. Sakama, M. Schädel, J. V. Kratz, H. Gäggeler, A. Türler, *J. Nucl. Radiochem. Sci.* **2002**, *3*, 85.

8 M. Plaisance, R. Guillaumont, *Radiochim. Acta* **1969**, *12*, 32.

9 S. Ahrland, D. Karipides, B. Norén, *Acta Chem. Scand.* **1963**, *17*, 411.

10 B. Norén, *Acta Chem. Scand.* **1967**, *21*, 2449.

11 E. L. Zebroski, H. W. Alter, F. K. Heumann, *J. Am. Chem. Soc.* **1951**, *73*, 5646.

12 R. D. Shannon, *Acta Cryst.* **1976**, *A32*, 751.

13 V. Pershina, D. Trubert, C. Le Naour, J. V. Kratz, *Radiochim. Acta* **2002**, *90*, 869.

Published on the web (Advance View) February 9, 2008; doi:10.1246/cl.2008.288

Available online at www.sciencedirect.com
ScienceDirect
Geochimica et Cosmochimica Acta 71 (2007) 3458–3475
Geochimica et Cosmochimica Acta
www.elsevier.com/locate/gca

Comparison of reductive accumulation of Re and Os in seawater–sediment systems

Yoshiro Yamashita [a], Yoshio Takahashi [a,*], Hiromitsu Haba [b], Shuichi Enomoto [b], Hiroshi Shimizu [a]

[a] *Department of Earth and Planetary Systems Science, Graduate School of Science, Hiroshima University, Higashi-Hiroshima, Hiroshima 739-8526, Japan*

[b] *RIKEN (The Institute of Physical and Chemical Research), Wako, Saitama 351-01, Japan*

Received 3 April 2006; accepted in revised form 3 May 2007; available online 10 May 2007

Abstract

In order to understand the fractionation of Re and Os in marine environments, their removal from artificial seawater to Tokyo Bay sediments is studied using a multitracer technique. The chemical processes of the removal of Re and Os are also estimated based on their speciation analyses by X-ray absorption fine structure (XAFS) spectroscopy. The partitioning experiments, which use the multitracer technique, provide information on Re and Os regarding (i) their distributions between artificial seawater–sediment systems, (ii) their complexation with humic acid, and (iii) their carriers in sediments. In addition, XAFS spectroscopy provides direct information on the chemical states of Re and Os in the sediments.

In an artificial seawater–sediment system containing a multitracer, Re is removed from the artificial seawater only under a reducing environment. The speciation of Re by X-ray absorption near-edge structure (XANES) suggests that the majority of Re remains as ReO_4^- in the artificial seawater even under highly reducing conditions, during laboratory time scale (about 2 weeks). Moreover, XANES simulation shows that some Re exists at a lower oxidation state, such as ReO_2, in the reducing sediment. These results can be explained by the slow kinetics of the reaction which is similar to those suggested by previous geochemical studies.

In contrast, Os is readily removed from the artificial seawater into sediments under various redox conditions. Even under oxic conditions, a large fraction of Os is removed from the artificial seawater to sediments without organic matter. Based on the Os XANES study, it is confirmed that the oxidation states of Os incorporated in the reducing sediment and oxic sediment are trivalent and tetravalent, respectively. Sequential extraction suggests that the main carrier of Os in the organic-rich sediment is either ferromanganese oxides or organic matter, and that the Os in these two fractions may correspond to hydrolyzed insoluble Os species and Os species interacting with organic matter, at lower valence, respectively. The results of distribution study of Os in the absence and presence of humic acid (HA) also imply that Os assumes more than one chemical species, and a small fraction of Os may interact with HA in the experimental system. Meanwhile, extended X-ray absorption fine structure (EXAFS) confirms that the first neighboring atom of Os in the reducing sediment is oxygen. If Os(VIII) is the main dissolved species in seawater, as is expected thermodynamically, reductive removal may control the enrichment of Os in the sediment. Osmium, which is removed as Os(IV), is reduced further to Os(III) by a diagenetic process and may be complexed with organic matter in the reducing sediment.

The results of the removal behaviors of Re and Os obtained in the current study show that Re can be removed from the artificial seawater only under highly reducing conditions within 2 weeks, but Os removal from the artificial seawater can be found under various redox conditions. Thus, a high $^{187}Re/^{188}Os$ ratio can occur only in reducing sediments, such as black shales. The high $^{187}Re/^{188}Os$ ratio, in turn, makes black shales suitable for Re–Os dating. In contrast, authigenic sediments (and minerals) under oxic environments can enrich Os, but since Re is not distributed to the sediments under oxic conditions,

* Corresponding author. Fax: +81 82 424 0735.
E-mail address: ytakaha@hiroshima-u.ac.jp (Y. Takahashi).

0016-7037/$ - see front matter
doi:10.1016/j.gca.2007.05.003

this will cause a much lower $^{187}Re/^{188}Os$ ratio than that of seawater. The Os isotope system of these materials can be used as a paleo-marine environmental tracer since the $^{187}Os/^{188}Os$ ratio cannot grow significantly due to its extremely low $^{187}Re/^{188}Os$ ratio.

1. INTRODUCTION

Osmium (Os), a platinum group element (PGE), is one of the least abundant elements on the earth's surface. Over the past 20 years, it has attracted considerable attention from geochemists due to the variability of its isotopic system, as the decay of ^{187}Re to ^{187}Os (half-life = 41.6 Gy, Smoliar et al., 1996) gives rise to subsequent variations in the Os isotopic composition. As a result of large Re–Os fractionation during geological processes, the Os isotope ratio becomes highly variable as compared to that of other isotopic systems. Consequently, the $^{187}Os/^{188}Os$ ratio is often employed as a potentially powerful isotopic tracer on material cycling in the surface environment (Ravizza et al., 1996; Sharma et al., 1997; Levasseur et al., 2000; Dalai et al., 2005). In addition, the ^{187}Re–^{187}Os system can also be applied as a geochronometer to organic-rich sedimentary rocks such as black shales (Ravizza and Turekian, 1989; Cohen et al., 1999; Selby and Creaser, 2003), sulfide minerals rich in Re such as molybdenite (Suzuki et al., 1993), and iron meteorites (Smoliar et al., 1996).

Despite the frequent utilization of ^{187}Re–^{187}Os, the geochemical behavior of Os in the surface environment, especially in marine environments, is largely unknown. This is because the Os concentration in seawater is extremely low, and the chemical treatment of its natural samples for mass spectroscopic analysis is not very straightforward due to the varied oxidation states of Os (Sharma et al., 1997; Levasseur et al., 1998; Woodhouse et al., 1999). Furthermore, the dissolved species and residence times of Os in marine environments are subject to debates (Levasseur et al., 1998; Oxburgh, 1998; Woodhouse et al., 1999).

On the other hand, it is widely known that both Re and Os are enriched in reducing sediment and that their concentrations correlate well with total organic carbon contents (Ravizza et al., 1991). It is considered that significant removal of these elements from seawater to sediment occurs in reducing marine environments. However, the removal mechanisms of Re and Os from seawater are not yet fully understood, and differences in the removal mechanisms of these two elements should induce large variations in the Re/Os ratio in sediments. So far, the geochemical behaviors of Re and Os have not been studied simultaneously by systematic experiments focusing on each chemical process. This study is, to our knowledge, the first report focusing on the removal of Re and Os from seawater to sediment and their chemical species in sediments by using two methods, namely, the multitracer technique and X-ray absorption fine structure (XAFS).

In this study, the multitracer technique, a carrier-free multi-radiotracer technique (Ambe et al., 1995; Ambe, 1996), was applied in order to understand the behaviors of Re and Os in seawater–sediment systems. The main advantage of this technique is that it gives direct information on the partitioning of Re and Os at concentration levels similar to those found in the natural marine environment. The concentration of radioactive tracers, such as ^{183}Re and ^{185}Os, is about 10^{-13} M in each experimental system, while the concentration of Re and Os in natural seawater is about 4.4×10^{-11} M and 4.2×10^{-14} M, respectively (Peucker-Ehrenbrink and Ravizza, 2001). However, a significant limitation of this technique is that it provides no constraints on the speciation of Re and Os. Thus, the XAFS technique was applied to the current study so that it can provide direct information on the chemical states of Re and Os incorporated within the sediment prepared in laboratory experiments. Both XANES and EXAFS can provide direct constraints on the oxidation state and local coordination environment (such as the neighboring atom and interatomic distance), respectively. However, the relatively lower sensitivity of this method required working at concentration levels of about 6–7 orders of magnitude higher than that found in the natural marine environment. In this combined study, the reasonable coherence of the results from the two approaches indicates that the constraints on Re and/or Os speciation obtained at a higher concentration can be reasonably extended to the much lower levels found in nature.

Here, these two methods are applied to several chemical processes during the removal of Re and Os to sediments in laboratory experiments. A conceptual diagram showing the purposes of individual experiments and their mutual relationship is given in Fig. 1. The experimental process and the results of the two approaches will be dealt with by dividing these into two sections and combining the results of both types of experiments in Section 4.

2. XAFS STUDY

In this chapter, the chemical speciation of Re and Os in sediments, such as their oxidation states and coordinate environments, is discussed based on XAFS.

2.1. XAFS experiments

The Re reference materials for XAFS analysis, namely, ReO_4^- solution, ReO_2, ReS_2, and Re metal, were obtained commercially. The osmium tetraoxide solution (OsO_4), $(NH_4)_2OsCl_6$, $OsCl_3$, $OsO_2 \cdot nH_2O$, OsS_2, and Os metal were used as Os reference materials. Perrhenate (ReO_4^-), OsO_4, and $(NH_4)_2OsCl_6$ were purchased from Kanto Chemical Co. Ltd. By adding OH^-, $OsO_2 \cdot nH_2O$ was synthesized from $OsCl_6^{2-}$ (Cotton and Wilkinson, 1987). For Os sulfide reference material, erlichmanite (OsS_2) was synthesized by following a previously reported procedure (Hayashi et al., 2000). All of the other reference materials were purchased from Rare Metallic Co. Ltd.

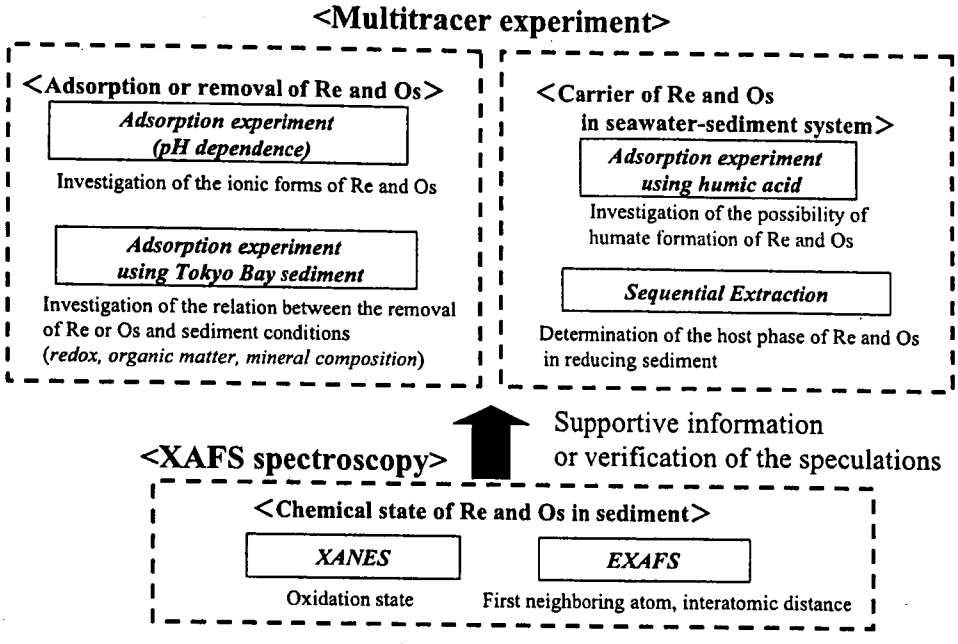

Fig. 1. Conceptual diagram for the purpose of individual experiments and the relation between each experiment.

The solid reference materials were diluted to 1 wt% by adding boron nitride or SiO_2 powder before pressing them into pellets. The sediment sample employed in this study was recovered from Tokyo Bay (N35°36.6′, E140°01.4′; 10 m depth). The sediment contained a high amount of organic C (2.07%) which was measured using a CHNS/O analyzer (Perkin Elmer 2400II). The other chemical composition of the sediment is shown in Appendix A. In order to investigate the effect of redox conditions on the oxidation states of Re and Os, untreated sediment (reducing) and air-dried sediment (oxic) were prepared (see Section 3.3.1). The weighed untreated or air-dried Tokyo Bay sediment (4.0 g) was flooded with 7.0 g of artificial seawater (see the Appendix A for the chemical composition) containing ReO_4^- (125 mg/dm^3) and either $OsCl_6^{2-}$ (62.5 mg/dm^3) or OsO_4 (250 mg/dm^3) in a polystyrene beaker with a cap. The beaker was then shaken for 2 weeks. In order to promote reduction, glucose (0.5 wt%) was added to the aqueous phase for some of the experimental systems (Rudolph et al., 1996). Here, $OsCl_6^{2-}$ and/or OsO_4 were used as the initial Os species in the artificial seawater, since they have been proposed to be the main Os species in seawater according to Koide et al. (1991), Brookins (1988). On the other hand, ReO_4^- was used as Re dissolved species in seawater (Brookins, 1988; Colodner et al., 1993, 1995). After incubation, the pH and Eh of the experimental system were measured using a glass electrode (Horiba, D-51) and a Pt electrode (Fujiwara, EHS-120). According to the partitioning coefficients of Re and Os obtained from the multitracer experiment, the concentrations of Re and Os in the sediments were estimated to be about 40 mg/kg and 100–400 mg/kg, respectively. The liquid phase was extracted as much as possible using a soil water sampler (Fujiwara, FV-448), and the sediment was packed in a polyethylene bag for XAFS measurements under an Ar atmosphere. After packing, the sediment samples were stored below −20 °C to prevent any chemical change during their storage until the XAFS measurement. The measurement and the analytical procedures of XAFS are shown in Appendix B.

2.2. Results of the XAFS study

The redox potentials of each experimental system for the XAFS experiment are summarized in Table 1. UTS (UnTreated Sediment) refers to untreated Tokyo Bay sediment incorporating Re and Os without the addition of glucose, while UTS-G (UnTreated Sediment with Glucose) indicates that with glucose. ADS (Air-Dried Sediment) indicates the air-dried Tokyo Bay sediment system without glucose. For Os in untreated sediment systems, three samples were prepared for each of UTS-G (OsO_4) and UTS-G ($OsCl_6^{2-}$), and the most and least reducing samples among the three was used for the XAFS measurement. The OsO_4 and $OsCl_6^{2-}$ in the parentheses show the initial Os species in the sorption study for XAFS measurement. Significant Eh decreases induced by microbial activity were observed for the untreated sediment systems. The pH decrease, with the progress of reducing conditions, was also observed for the experimental systems using untreated and dried sediments. Similar pH decreases were thermodynamically calculated for natural reducing environments, such as the Black Sea (Van Cappellen and Wang, 1996). Since the Eh value depends on pH, a simple comparison among the raw Eh values of each sediment cannot reveal the intrinsic difference among the redox conditions of each sediment. Following Bohn (1971), Megonigal et al. (1993), the Eh value was corrected to Eh*, the Eh value at pH 8 in each system (Eh*/mV = Eh/mV − (8-pH) × 59), in order to simplify the discussion. Table 1 includes the corrected Eh* and raw Eh–pH data. As shown in Table 1, Eh* in glucose-free or

Table 1
Eh–pH conditions of sediment samples (Tokyo Bay sediment) after 2 weeks of incubation for the XAFS measurement

Sample	Initial state	Sediment	Glucose (wt%)	pH	Eh (mV)	Eh* (mV)
Rhenium						
UTS-G (ReO_4-)	ReO_4^-	Untreated	0.5	5.2	−108	−273
UTS (ReO_4-)	ReO_4^-	Untreated	0.0	4.3	345	127
Osmium						
UTS-G1 ($OsCl_6^{2-}$)	$OsCl_6^{2-}$	Untreated	0.5	5.4	−35	−188
UTS-G2 ($OsCl_6^{2-}$)	$OsCl_6^{2-}$	Untreated	0.5	6.0	−127	−245
UTS-G1 (OsO_4)	OsO_4	Untreated	0.5	5.0	27	−150
UTS-G2 (OsO_4)	OsO_4	Untreated	0.5	4.9	−120	−303
ADS ($OsCl_6^{2-}$)	$OsCl_6^{2-}$	Air-dried	0.0	7.4	193	357
ADS (OsO_4)	OsO_4	Air-dried	0.0	7.2	222	374

Glucose was added to the aqueous phase of the seawater–sediment system to promote a reducing condition. The initial pH was adjusted to 8.0, which decreased with the progress of microbial-mediated reduction as described in Van Cappellen and Wang (1996).

air-dried sediment systems did not significantly decrease after incubation for 2 weeks.

The loading levels of Re and Os in artificial seawater were about 6–7 orders of magnitude higher than those in natural seawater. Therefore, there is the possibility that the speciation of Re and Os by XAFS does not reflect the natural speciation of both elements. However, as described in subsequent sections, the results of XAFS are likely to be reasonable because (i) the speciation by XAFS is consistent with the results of the distribution study using the multitracer technique, and (ii) the distribution ratios of Re and Os tracers are similar to those observed in nature.

2.2.1. *XANES spectra for Re*

Re L_{III}-edge XANES spectra of some reference materials and Re adsorbed on the sediment, along with the spectrum for Re in the artificial seawater recovered from the sediment, are shown in Fig. 2. As the oxidation state of Re becomes larger, the spectra of reference materials show that the absorption edge shifts to higher energy. This phenomenon (chemical shift) is commonly observed with many elements; it can be explained by the larger attraction forces between a nuclei and an inner electron for the ion at a higher oxidation state (Iida, 2000). Therefore, the oxidation state of Re adsorbed on sediments can be obtained from its peak energy by comparing it with that of the reference materials.

The XANES spectra of Re adsorbed on sediments and in the artificial seawater were quite similar to those of ReO_4^- in terms of the peak energy and spectral shape (Fig. 2). These results suggest that even under highly reducing conditions, not all Re was reduced as seen in the sample UTS-G (ReO_4^-). However, the peak energy of this sample shifted to a slightly lower energy than those of ReO_4^- and UTS (ReO_4^-). This result indicates that the redox condition of this sample (Eh* = −273 mV, measured Eh = −108 mV at pH 5.2) reached the theoretical reducing potential of the ReO_4^-/ReO_2 couple (Eh = −235 mV at pH 8 and total Re = 10^{-6} M: Brookins, 1988). The observation that the reduction of ReO_4^- to lower stable oxidation states, such as ReO_2 (or other tetravalent Re species), was not completed under highly reducing condition (our S K-edge XANES study shows that the main S species in UTS-G is sulfide) which indicates that the reduction process of ReO_4^- is relatively slow. At the least, the reduction of ReO_4^- cannot be attained within 2 weeks, even if the redox potential is sufficiently decreased compared to the reducing potential of ReO_4^-.

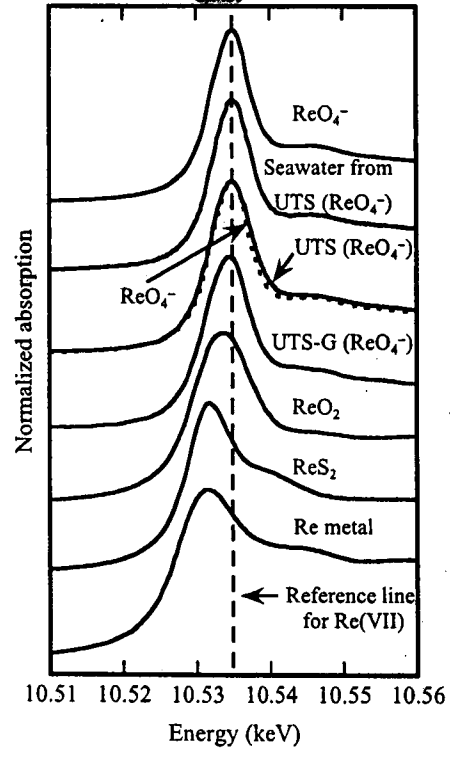

Fig. 2. Rhenium L_{III}-edge XANES spectra for reference materials (ReO_4^-, ReO_2, ReS_2, and Re metal), Re on sediment samples, and Re in artificial seawater recovered from the experimental system of the oxic sediment (UTS (ReO_4^-)). Following Bohn (1971) and Megonigal et al. (1993), the Eh values for each experiment were corrected to the values at pH 8 (Eh*). The Eh* and measured Eh–pH conditions for each sample are summarized in Table 1. The spectrum of ReO_4^- overlapped with that of UTS (ReO_4^-).

To investigate the contribution of Re(IV) in the sample UTS-G (ReO_4^-), the XANES spectrum for the sample was simulated by those of ReO_4^- and ReO_2 (Fig. 3). The

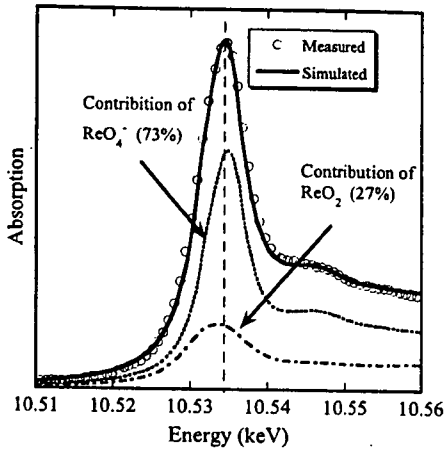

Fig. 3. Simulation of Re L_{III}-edge XANES by the spectra of ReO_2 and ReO_4^-. Open circle: sediment spectrum (UTS-G (ReO_4^-)); solid: fitted spectrum using the normalized spectra for ReO_4^- and ReO_2; dashed: the contributions of ReO_4^- and ReO_2.

simulation was able to explain the sample spectrum, and the contributions of ReO_4^- and ReO_2 were estimated to be 73% and 27%, respectively. This result suggests that the primary and secondary oxidation states of Re in the reducing sediments are Re(VII) and Re(IV), respectively.

2.2.2. XANES spectra for Os

Fig. 4 shows the Os L_{III}-edge XANES spectra of some reference materials and Os adsorbed on sediments. Two reducing sediment samples, a highly reducing one (UTS-G2) and a less reducing one (UTS-G1), were prepared.

As seen in Fig. 4, irrespective of the initial species (OsO_4 or $OsCl_6^{2-}$) introduced into the artificial seawater and the degree of the development of the reducing condition ($Eh^* < -100$ mV), the peak energies of the XANES spectra for Os adsorbed on all UTS-G series samples were similar to those of $OsCl_3$. This result indicates that Os adsorbed on the reducing sediment is mainly in a trivalent state. Since the initial oxidation state of Os was tetravalent or octavalent, it is confirmed that Os is incorporated into reducing sediments through reductive reactions.

On the other hand, the peak energy of Os adsorbed on air-dried sediment, ADS ($OsCl_6^{2-}$ or OsO_4), shifted to a higher energy and nearly coincided with that of $OsO_2 \cdot n$-H_2O. The Eh^* values of these sediments were about 350 mV, and, as with reducing sediment samples, significant differences between the energies of absorption peak related to the initial species ($OsCl_6^{2-}$ or OsO_4) were not observed in these samples. These results suggest that Os can be removed from seawater as Os(IV) at the first step. If the Os(VIII) oxyanion is assumed to be the dissolved species in seawater, chemical reduction is an important factor for the removal of Os. On the other hand, if Os(IV) is the dissolved species in seawater, chemical reduction is not important for the removal of Os under oxic conditions. Alternatively, ligand exchange from chlorine to oxygen can occur for Os(IV) without reduction. Following adsorption on sediment as Os(IV), Os(IV) can be reduced to Os(III) by diagenetic processes in the reducing sediment. This suggestion can be confirmed by the fact that the XANES spectra of the ADS series have a shoulder at the absorption peak of Os(III), showing that the ADS series contains Os(IV) and other species at lower oxidation states. The XANES spectra of the UTS-G series samples are dissimilar to those of $Os(II)S_2$ (Fig. 4), confirming that further reductive reactions from the Os(III) species to OsS_2 or Os metal could hardly proceed. The current S XANES study suggested that the main S species of the UTS series is sulfide (=98%, data not shown). Thus, Os sulfide species do not seem to be important (for any valence) in a reducing sediment system. Since the chemical shift was observed between the ADS series and UTS-G series samples, it is confirmed that the primary and secondary species of Os in marine sediments are Os(III) and Os(IV), respectively, and that the Os(III)/Os(IV) ratio may change as a function of the sediment redox condition.

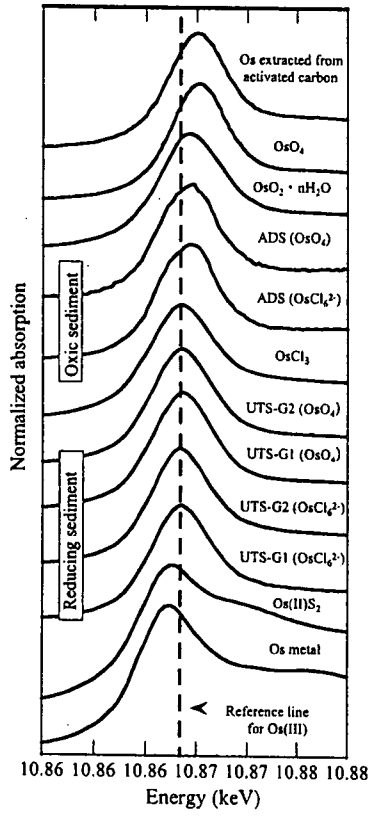

Fig. 4. Osmium L_{III}-edge XANES spectra for reference materials (OsO_4, $OsO_2 \cdot nH_2O$, $OsCl_3$, OsS_2, and Os metal), Os extracted from activated carbon and Os on sediment samples. The Eh^* and measured Eh–pH conditions for each sample are summarized in Table 1.

2.2.3. EXAFS spectra of Os in sediments

Here, the EXAFS regions of Os in sediments are compared with those of some of the reference materials in order to obtain information on detailed species or specific structures of Os adsorbed on reducing sediments, UTS-G2 ($OsCl_6^{2-}$ or OsO_4). In addition, the EXAFS for reference

materials and UTS-G2 series samples were fitted using parameters generated by FEFF7.0.

Fig. 5 shows the k^3-weighted EXAFS function $\chi(k)$ of Os in the reducing sediments and some Os reference materials. The EXAFS functions of Os bound to Cl or S are similar to each other, but are clearly different from that of $OsO_2 \cdot nH_2O$. The EXAFS function of $OsO_2 \cdot nH_2O$ is characterized by its large amplitude observed in the lower k region ($k < 5$ Å^{-1}) as compared to that of $OsCl_6^{2-}$ or OsS_2. The structures in the EXAFS functions for both UTS-G2 samples are consistent with that of $OsO_2 \cdot nH_2O$. As was seen in the XANES spectra, the EXAFS functions for Os in these two sediments are similar to each other in spite of their different initial chemical forms ($OsCl_6^{2-}$ or OsO_4).

Radial structural functions (RSF) of Os contained in the above sediments and Os reference materials are shown in Fig. 6. The $R+\Delta R$ (Å) of a first Fourier Transformation (FT) peak reflects the approximate interatomic distance (+ phase shift) between Os and the first neighboring scattering atom. The first FT peak of reference materials obviously follows the order of the ionic radii of coordinated

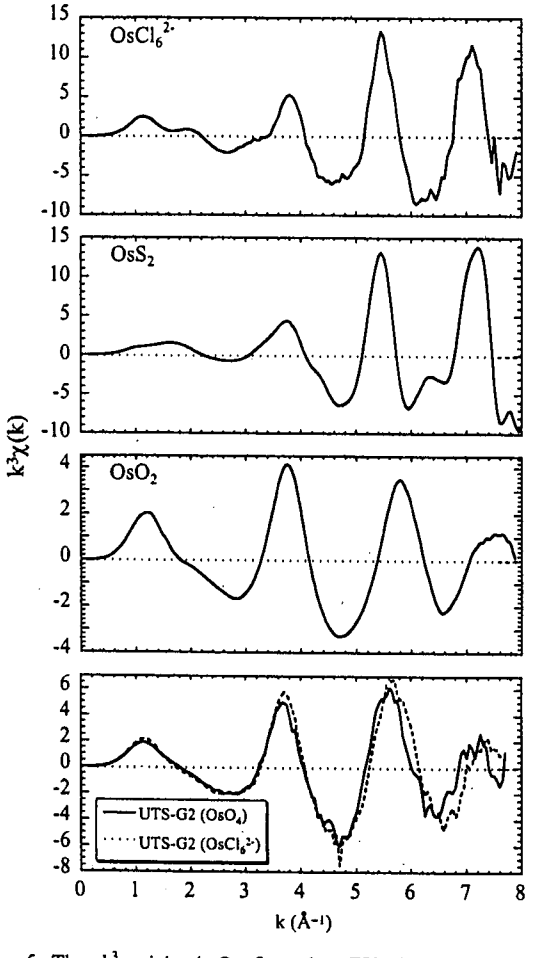

Fig. 5. The k^3-weighted Os L_{III}-edge EXAFS functions for reference materials ($OsCl_6^{2-}$, $OsO_2 \cdot nH_2O$, and OsS_2) and sediment samples. The sediment samples are UTS-G2 (OsO_4) and UTS-G2 ($OsCl_6^{2-}$) in Fig. 3.

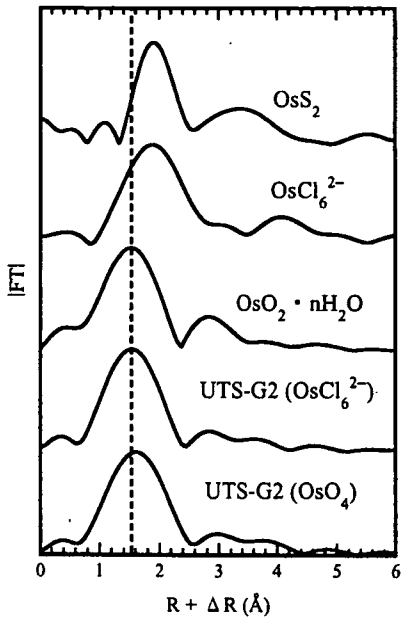

Fig. 6. Radial structure functions (RSF) for reference materials ($OsCl_6^{2-}$, $OsO_2 \cdot nH_2O$, and OsS_2), UTS-G2 (OsO_4), and UTS-G2 ($OsCl_6^{2-}$). The phase shift was not corrected.

atoms ($O^{2-} < Cl^- < S^{2-}$; Shannon, 1976). These results suggest that the first neighboring atom of Os in the sediments can be distinguished by comparing the $R + \Delta R$ (Å) of the first peak with the reference materials. Since the $R + \Delta R$ (Å) of the first FT peak of Os in the sediment agrees with that of $OsO_2 \cdot nH_2O$, the neighboring atom is likely to be oxygen.

The fitting parameters obtained here are shown in Table 2. To verify the quality of the simulation, reference materials were fitted in a way which is similar to Os in the sediments. The calculated interatomic distances for the Os–Cl ($OsCl_6^{2-}$), Os–O (OsO_2), and Os–S (OsS_2) bonds for the reference materials are 2.316, 1.963, and 2.350 Å, respectively ($N = 6$). These results are comparable with previous reports; the ideal interatomic distances for Os–Cl bond in $OsCl_6^{2-}$, Os–O bond in OsO_2, and Os–S bond in OsS_2 are 2.261, 1.961, and 2.351 Å, respectively (Boman, 1970; Cotton and Rice, 1977; Stingl et al., 1992). Therefore, the quality of the XAFS measurements and EXAFS analysis results using FEFF7.0 is acceptable. The fitting parameters for Os in the sediments, obtained by curve fitting, when the neighboring atom of Os was assumed to be Cl, O or S, are also shown in Table 2. When Cl or S was assumed to be the first neighboring atom of Os for the two sediment samples of UTS-G2 (OsO_4) and UTS-G2 ($OsCl_6^{2-}$), it becomes apparent that the calculated interatomic distances of Os–Cl (2.149–2.186 Å) and Os–S (2.168–2.217 Å) bonds were shorter than those expected from the analyses of reference materials. In contrast, when O was assumed to be the first neighboring atom of Os, the interatomic distances (1.984 or 2.017 Å) obtained for both sediments become comparable to that of the Os–O bond (1.961 Å) in a previous report (Boman, 1970).

Table 2
EXAFS fitting parameters using FEFF7.0 for $OsCl_6^{2-}$, $OsO_2{\cdot}nH_2O$, OsS_2, Os adsorbed on sediment from OsO_4 solution or $OsCl_6^{2-}$ solution

Sample	Shell	N	R(Å)	dE (eV)	DW	Residual (%)
$OsO_2 \cdot nH_2O$	Os–O	6	1.963 (0.004)	8.1 (0.4)	0.130 (0.006)	0.134
$OsCl_6^{2-}$	Os–Cl	6	2.316 (0.002)	8.1 (0.2)	0.061 (0.006)	0.208
OsS_2	Os–S	6	2.350 (0.003)	7.4 (0.4)	0.054 (0.004)	1.060
UTS-G2 (OsO_4)	Os–O	6	1.984 (0.002)	7.1 (0.2)	0.072 (0.005)	0.746
	Os–Cl	6	2.149 (0.003)	−4.7 (0.4)	0.117 (0.005)	0.329
	Os–S	6	2.168 (0.003)	−6.7 (0.3)	0.113 (0.006)	0.381
UTS-G2 ($OsCl_6^{2-}$)	Os–O	6	2.017 (0.004)	8.2 (0.4)	0.085 (0.008)	0.865
	Os–Cl	6	2.186 (0.003)	−2.7 (0.4)	0.125 (0.005)	0.699
	Os–S	6	2.217 (0.003)	−3.1 (0.4)	0.120 (0.007)	0.266

The first neighboring atom of Os in the sediments was assumed to be O, Cl, and S. N, coordination number fixed at 6 in this simulation; R (Å), interatomic distance; dE: threshold E_0 shift in eV; DW, Debye–Waller factor. The least squares precisions are given in parentheses. The accuracy of the fitted parameters was estimated to be generally ±0.02 for R (Å), and ±20% for DW (O'Day et al., 1994).

The EXAFS results reveal that the first neighboring atom of Os in the sediment is O and that the interatomic distance of the Os–O bond ranges from 1.984 to 2.017 Å. A slightly larger Os–O distance than OsO_2 (1.961 Å) suggests that Os(III)–O bonding is formed in the sediments because the ionic radius (r) generally becomes longer at a lower oxidation state ($r_{Os(IV)} < r_{Os(III)}$). This suggestion is partly supported by the XANES study, which indicates that Os(III) and Os(IV) coexist in these sediment systems, though a thorough confirmation of this result is not possible because Os_2O_3 is poorly characterized in the literature.

3. MULTITRACER STUDY

In this chapter, (i) the ionic forms of dissolved Re and Os in artificial seawater, (ii) Re and Os removal from artificial seawater to various sediments (untreated-, dried-, burnt-, and oxidized-sediments), (iii) the possibility of humate formation for Re and Os, and (iv) the host phase of Re and Os in artificial seawater–sediment system are discussed using the multitracer technique.

3.1. Preparation of the multitracer

Various radioisotopes, including ^{183}Re and ^{185}Os in the multitracer, were produced by the nuclear fragmentation reaction between Au target and heavy ions (^{12}C, ^{14}N, or ^{16}O) accelerated by RIKEN Ring Cyclotron in Wako, Japan (Ambe et al., 1995). The Au foil irradiated with the heavy ions was dissolved with aqua regia.

From the Au target, ^{185}Os and ^{183}Re were recovered. Since Os is easily oxidized with nitric acid to a highly volatile and strongly oxidizing octavalent state, dissolution of the Au foil containing ^{185}Os isotopes was performed in a closed system using a rotary evaporator. An activated carbon column was connected between the evaporator and an aspirator in order to recover the volatile Os, and the Os was extracted from the activated carbon by boiling it with 30 wt% H_2O_2 at 100 °C. From the residual solution containing Au and other radioisotopes, Au (matrix element) was removed by solvent extraction with ethyl acetate. Rhenium-183 was obtained from the water phase through the anion exchange method. The final working solutions were then prepared by adding a few microliter of the original multitracer solution to the working solution (artificial seawater, humic acid solution, and MQ water) followed by pH adjustment in every experiment. The speciation of various elements, except for Re and Os, in the original multitracer solution was documented by Takahashi et al. (1997, 1999). The speciation of Re and Os in the initial solution will be discussed later.

3.2. Adsorption onto various adsorbents

In this section, the ionic forms of the Re and Os ions in artificial seawater are investigated by adsorption experiments. Combining the results of XANES, the species of Re and Os in artificial seawater are estimated.

3.2.1. Experimental process

The adsorption of Re and Os on several adsorbents, such as hematite (Rare Metallic Co. Ltd.), ferromanganese oxide prepared as a powder of ferromanganese nodules (JMn-1: Geological Survey of Japan), silica gel (Fuji Division Chemicals Ltd.), and anion exchange resin (AG1-X8: Bio-Rad Laboratories), were examined under a wide range of pH conditions. Each adsorbent (0.5 g) was mixed with 7.0 g of artificial seawater containing multitracer in a polystyrene beaker with cap. After adjusting the pH of the solution with a small amount of NaOH or HCl solution, the suspension was shaken for 30 min. After centrifugation, the supernatant was recovered by filtration (0.45 μm). The γ-ray spectrum of radioisotopes in the filtrate was recorded using a pure Ge detector (GEM15P, Seiko EG&G) coupled with a multichannel analyzer. The γ-ray peaks were assigned to each radioisotope based on their half-lives and the energies of the photoelectric peaks. The peak area was computed using a routine program. The dissolved fraction of each element was calculated by comparison with a standard solution containing an identical amount of the multitracer, while the dissolved percentage of a radioisotope (R) was calculated by comparing the intensity of its peak for the sample (S_1) with that of the standard solution (S_0):

$$R(\%) = 100\, S_1/S_0 \quad (1)$$

The volumes of the sample and standard solution were kept constant at 3.0 ml to eliminate the effect of geometry on the Ge detector. Estimated from the radioactivity and the detection efficiency of the Ge detector, the concentrations of all of the radioisotopes in each experimental system were less than 10^{-13} M.

3.2.2. Adsorption onto various adsorbents

The adsorption of the multitracer on several adsorbents under various pH conditions is shown in Fig. 7. Without adsorbents, Re and Os were not removed, indicating that they are dissolved in the aqueous phase, and thus their removal by precipitation and adsorption on the walls of the polystyrene beaker can be ignored. After a contact time of 30 min, both Re and Os were significantly adsorbed on the anion exchange resin in the whole pH range, but their adsorption on silica, hematite, and ferromanganese oxide was minimal. On the other hand, Takahashi et al. (1999) reported that various cationic species were adsorbed on silica gel in a similar experimental system.

The surface charge of each adsorbent changes as a function of pH. Under acidic to neutral pH conditions, Mn and Fe oxides have positive charges, which turn into negative charges under neutral to basic pH conditions (Langmuir, 1997). On the other hand, the surface charges of silica and anion exchange resin are constantly negative and positive, respectively, under a wide pH region. The results of the adsorption experiment suggest that Re existed in an anionic form in artificial seawater. This result is consistent with previous studies that ReO_4^- is a stable species in the aqueous phase (Baes and Mesmer, 1986; Brookins, 1988). Furthermore, this suggestion is supported by XANES, the results of which reveal that Re was dissolved as ReO_4^- in artificial seawater (Fig. 2).

The results of the adsorption experiment further suggest that Os is also dissolved in an anionic form in artificial seawater. Moreover, the XANES results show that Os extracted from activated carbon is octavalent (Fig. 4). Combining the results of XANES and the adsorption experiment using various adsorbents, the initial state of Os in artificial seawater used in the multitracer experiments was estimated to be the Os(VIII) anionic species, which are more specifically either $HOsO_5^-$ or $H_2OsO_6^-$.

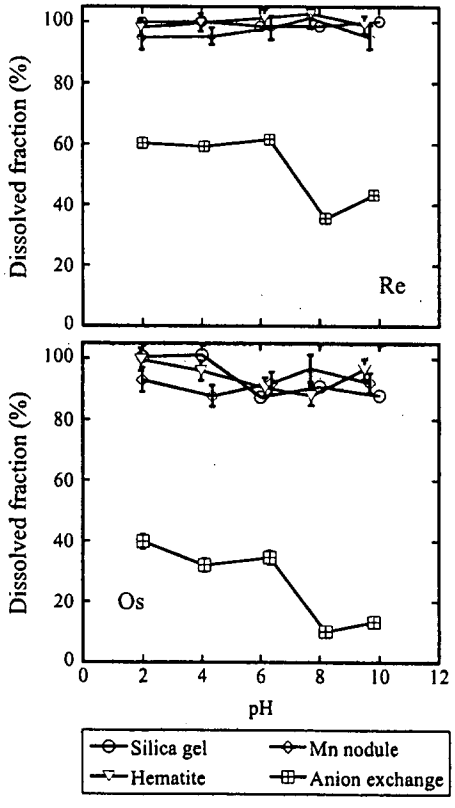

Fig. 7. Adsorption of Re and Os on various adsorbents (silica gel, ferromanganese oxide, hematite, and anion exchange resin). The pH_{ZPC} (point of zero charge) are 2.5, 2.5, and 6–8 for silica, ferromanganese oxide, and hematite, respectively (Langmuir, 1997).

3.3. Adsorption experiment onto Tokyo Bay sediments

In this section, the relationship between the removal behaviors of Re and/or Os on Tokyo Bay sediments and the condition of the sediments (such as redox potential, with or without organic matter, and mineral composition) using the multitracer technique is described.

3.3.1. Experimental process

The following sediment samples were prepared: (a) untreated sediment: containing a high proportion of organic carbon (2.07 wt%) which is un-oxygenated before the experiments, (b) air-dried sediment: containing a high proportion of organic carbon (2.07 wt%) which is well air-dried (well oxygenated at room temperature before the experiments), and (c-1) burnt sediment: burnt at 980 °C to decompose organic matter and sterilize microorganisms. "Oxidized sediment (c-2)" with 30 wt% H_2O_2 and 0.020 M HNO_3 for organic-free sediment was also prepared because the burning process decomposes the hydrous minerals, such as clay minerals, which are abundant in sediments and are important as sorption sites for metal ions. In experiments employing untreated sediment, the percentage of water content of the sediment was calculated in advance, and the weight ratio between the seawater and dry sediment was equalized among all four experimental systems. Weighed sediment (4.0 g) was flooded with artificial seawater (8.0 g) containing multitracer and adjusted to pH 8 in a polystyrene beaker with cap. In order to promote microbial activity (reducing condition), glucose (0.5 wt%) was added to the seawater of untreated- and dried-sediment systems following the method of Rudolph et al. (1996). The beaker was shaken constantly at 25 °C. At regular time intervals, the pH and Eh levels of the experimental system were measured, and 3.0 ml of seawater was recovered from the beaker to measure the γ-ray spectra after centrifugation. After the γ-ray measurements, each solution was returned to the original beaker.

3.3.2. Adsorption onto Tokyo Bay sediments

The results of the adsorption experiment using Tokyo Bay sediment are shown in Fig. 8, where the Eh* (and measured Eh–pH) change in each experimental system is also shown. In the untreated sediment system, Re was removed from artificial seawater to the sediment with an Eh decrease (Fig. 8a), but the dissolved fraction in the artificial seawater was still 81% at Eh* = −136 mV (measured Eh = −49 mV at pH 6.5). On the other hand, Re completely remained in the artificial seawater during the experimental period in the systems of dried-, burnt-, and oxidized- sediments (Figs. 8b, 8c-1, -2), where the Eh* value was larger than that in the untreated sediment (Eh* was 120, 470, and 348 mV for dried-, burnt-, and oxidized- sediments, respectively). That is, Re removal requires the development of reducing conditions in the presence of organic matter. However, a large amount of Re remained in the artificial seawater even in the untreated (reducing) sediment system. This is because the reducing potential of the ReO_4^-/ReO_2 couple is very low (e.g., reducing potential of Re(VII)/Re(IV) is about −274 mV at pH 8 and total Re = 10^{-8} M: Brookins, 1988), and the kinetics of ReO_4^- reduction may be slow, as indicated by the results of XAFS. Based on this adsorption experiment, it can be seen that the redox condition is an important factor in controlling the behavior of Re in a natural aquifer, and that Re is stable as a dissolved species (ReO_4^-) under reducing conditions, over a time scale of at least 2 weeks.

In contrast, a large amount of Os was removed from the artificial seawater to sediments in all systems (Fig. 8). For untreated-, dried-, and burnt-sediment systems, more than 80% of the total Os was incorporated into the sediments within 180 h (Fig. 8a–c1). The purpose of using untreated- and dried-sediment systems was to verify the removal behaviors of elements under highly reducing conditions with organic matter, and more oxic conditions with organic matter, respectively. In both experiments, Os was gradually removed from artificial seawater along with a microbially-mediated Eh* decrease. This result suggests that Os can be reduced to an insoluble form at a lower valence from the initial Os(VIII) dissolved species. This suggestion is somewhat reasonable because these sediments contain a

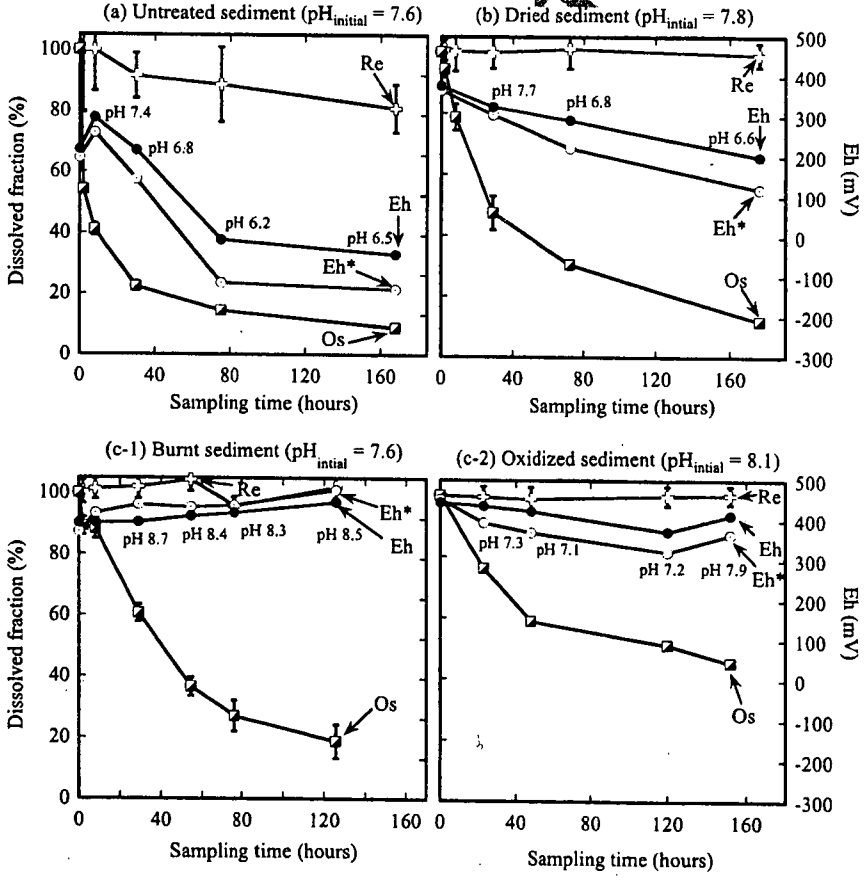

Fig. 8. Time-dependence of the removal of Re and Os from artificial seawater to sediment. The sediment samples are (a) untreated sediment, (b) dried sediment, (c-1) burnt sediment (980 °C), and (c-2) oxidized sediment (30% H_2O_2 and 0.02 M H_2NO_3). The removal patterns of Re and Os are shown as solid curves. The Eh* and measured Eh changes in each experimental system are also indicated by solid curves. The pH levels at the sampling times for each experimental system are shown in each figure. The average pH values for the systems were (a) 6.9, (b) 7.2, (c) 8.3, and (d) 7.4, respectively. For untreated sediment and dried sediment systems, the RSD (%) obtained from repeated experiments (n = 3) were less than 10%.